



# Visible, Near-Infrared, and Dual-Range Luminescence Spanning the 4f Series Sensitized by a Gallium(III)/Lanthanide(III) Metallacrown Structure

Elvin V Salerno, Svetlana Eliseeva, Bernadette L Schneider, Jeff W Kampf,  
Stephane Petoud, Vincent L Pecoraro

## ► To cite this version:

Elvin V Salerno, Svetlana Eliseeva, Bernadette L Schneider, Jeff W Kampf, Stephane Petoud, et al.. Visible, Near-Infrared, and Dual-Range Luminescence Spanning the 4f Series Sensitized by a Gallium(III)/Lanthanide(III) Metallacrown Structure. *Journal of Physical Chemistry A*, 2020, 124 (50), pp.10550-10564. <10.1021/acs.jpca.0c08819>. <hal-03037723>

**HAL Id: hal-03037723**

**<https://hal.science/hal-03037723v1>**

Submitted on 3 Dec 2020

**HAL** is a multi-disciplinary open access archive for the deposit and dissemination of scientific research documents, whether they are published or not. The documents may come from teaching and research institutions in France or abroad, or from public or private research centers.

L'archive ouverte pluridisciplinaire **HAL**, est destinée au dépôt et à la diffusion de documents scientifiques de niveau recherche, publiés ou non, émanant des établissements d'enseignement et de recherche français ou étrangers, des laboratoires publics ou privés.



HAL Authorization

# Visible, Near-Infrared, and Dual-Range Luminescence Spanning the 4f Series Sensitized by a Gallium(III)/Lanthanide(III) Metallacrown Structure

Elvin V. Salerno,<sup>‡</sup> Svetlana V. Eliseeva,<sup>\*,‡</sup> Bernadette L. Schneider, Jeff W. Kampf, Stéphane Petoud,<sup>\*</sup> and Vincent L. Pecoraro<sup>\*</sup>

**ABSTRACT:** Lanthanide(III) ions ( $\text{Ln}^{3+}$ ) in coordination compounds exhibit unique luminescent properties with narrow and characteristic f-f transitions throughout the visible and near-infrared (NIR) ranges. In addition, some  $\text{Ln}^{3+}$  such as  $\text{Pr}^{3+}$ ,  $\text{Sm}^{3+}$ ,  $\text{Dy}^{3+}$ ,  $\text{Ho}^{3+}$ ,  $\text{Er}^{3+}$  and  $\text{Tm}^{3+}$  possess an exceptional ability, although less explored, to exhibit dual-range emissions. Such remarkable features allow highly specific use in materials sciences and biology, for example, for the creation of sophisticated barcode modules or for the next generation of optical imaging applications. Herein, a series of  $\text{Ga}^{3+}/\text{Ln}^{3+}$  metallacrowns (MCs) with the general composition  $[\text{LnGa}_8(\text{shi})_8(\text{OH})_4]\text{Na}\cdot x\text{CH}_3\text{OH}\cdot y\text{H}_2\text{O}$  (**Ln-1**,  $\text{Ln} = \text{Pr}^{3+}$ ,  $\text{Nd}^{3+}$ ,  $\text{Sm}^{3+}$ – $\text{Yb}^{3+}$  and analogue  $\text{Y}^{3+}$ ;  $\text{H}_3\text{shi}$  = salicylhydroxamic acid) is presented. **Ln-1** were obtained by reacting  $\text{Ga}^{3+}$  and  $\text{Ln}^{3+}$  nitrate salts with the  $\text{H}_3\text{shi}$  ligand. X-ray single crystal unit cell analysis confirmed that all MCs are isostructural. The crystal structure was solved for the  $\text{Nd}^{3+}$  analogue and revealed that  $\text{Nd}^{3+}$  is centered between two  $[12\text{-MC}_{\text{Ga}^{\text{III}}\text{N}(\text{shi})\text{-4}}]$  MC rings and bound to eight hydroxamate oxygen ions (four from each ring) in a pseudo-square antiprismatic fashion adopting a pseudo- $D_{4h}$  symmetry. PGSE DOSY  $^1\text{H}$  NMR spectroscopy and ESI mass-spectrometry confirmed that the structure of **Ln-1** remains intact in methanol solutions while mass spectrometry suggests that four  $\text{OH}^-$  bridges are exchanged with  $\text{CH}_3\text{O}^-/\text{CD}_3\text{O}^-$ . An exceptional ability of this series of MCs to sensitize the characteristic emission of  $\text{Ln}^{3+}$  was confirmed with the observation of bright red and green emission signals of **Eu-1** and **Tb-1**, NIR emissions of **Yb-1** and **Nd-1**, and dual-range emissions of **Pr-1**, **Sm-1**, **Dy-1**, **Ho-1**, **Er-1** and **Tm-1** in the solid state upon excitation into ligand-centered bands at 340 nm. The luminescence properties of **Ln-1** ( $\text{Ln} = \text{Nd}^{3+}$ ,  $\text{Sm}^{3+}$ ,  $\text{Eu}^{3+}$ ,  $\text{Tb}^{3+}$ ,  $\text{Dy}^{3+}$ ,  $\text{Yb}^{3+}$ ) were also investigated in  $\text{CH}_3\text{OH}$  and  $\text{CD}_3\text{OD}$  solutions. For **Eu-1** and **Yb-1** MCs, more extensive analyses of the photophysical properties were performed that included the determination of radiative lifetimes, intrinsic quantum yields and sensitization efficiencies. The absolute quantum yields ( $Q_{\text{Ln}}^{\text{L}}$ ) of **Ln-1** in the visible and in the NIR ranges have been determined. In the case of **Sm-1** the values of  $Q_{\text{Ln}}^{\text{L}}$  in  $\text{CH}_3\text{OH}$  and  $\text{CD}_3\text{OD}$  solutions are exceptionally high, i.e. 10.1(5) % and 83(1) %. Values obtained for **Yb-1**, i.e. 0.78(4) % in  $\text{CH}_3\text{OH}$  and 8.4(1)% in  $\text{CD}_3\text{OD}$ , are among the highest ones reported today for  $\text{Yb}^{3+}$  complexes formed with non-deuterated and non-halogenated ligands.

## INTRODUCTION

Metallacrowns (MCs) constitute a class of supramolecular complexes which possess a  $[\text{M-N-O}]_n$  repeating ring motif.<sup>1-2</sup> The  $\text{M}^{n+}$  ring cations are usually 3d transition metal ions (from vanadium(V) to zinc(II)), but MCs with the group 13 triels such as gallium(III)<sup>3-6</sup> or with 4d and 5d transition metal ions (e.g. palladium(II), platinum(II))<sup>7</sup> have also been synthesized. Due to the diversity of structures and functional properties combined with the ease of synthesis via self-assembly in (typically) ambient temperature conditions MCs have found a broad range of applications in different fields such as molecular recognition,<sup>8-14</sup> molecular magnetism,<sup>15-23</sup> and magnetorefrigeration,<sup>24</sup> as well as contrast agents for magnetic resonance imaging (MRI)<sup>25-27</sup> or as luminescent probes for optical imaging.<sup>28-29</sup>

It has been shown that many MCs are able to bind a single or multiple trivalent lanthanide(III) ions ( $\text{Ln}^{3+}$ ).<sup>1</sup>  $\text{Ln}^{3+}$  are widely studied for their unique optical properties derived from core-like valence 4f orbitals. Since 4f orbitals are present within the 5s and 5p orbitals, they are largely shielded from crystal field and covalent bonding effects. Such electronic structure results in  $\text{Ln}^{3+}$  displaying narrow

and characteristic in their absorption and emission spectra from the corresponding f-f transitions, the positions of which are generally not significantly affected by the coordination environment or environmental conditions (e.g. pH, temperature, biomolecules).<sup>30</sup> The characteristic emission of  $\text{Ln}^{3+}$  compounds that cover UV, visible, and near-infrared (NIR) ranges lead to their various applications in materials science<sup>31</sup> and biology:<sup>32-33</sup> from telecommunications,<sup>34</sup> secret tags,<sup>35</sup> lighting, display technologies,<sup>36</sup> and night-vision devices<sup>37</sup> to optical imaging and sensing.<sup>38-41</sup> Although  $\text{Ln}^{3+}$  luminescence is widely used, f-f transitions suffer from low molar absorptivities ( $<10 \text{ M}^{-1}\text{cm}^{-1}$ ) due to the Laporte- and spin- forbidden nature of most of such transitions. This forbiddance leads to experimentally useful long-lived excited state lifetimes of  $\text{Ln}^{3+}$ , but, it implies that  $\text{Ln}^{3+}$  emission must be sensitized indirectly in order to obtain a significant emission intensity.<sup>30</sup> One of the strategies for  $\text{Ln}^{3+}$  sensitization is based on the ‘antenna effect’<sup>42</sup> that is typically achieved by surrounding  $\text{Ln}^{3+}$  with organic chromophoric ligands. As a general scheme, the energy is absorbed by the ligand through singlet states ( $\text{S}_0 \rightarrow \text{S}_n$ ), followed by internal conversion ( $\text{S}_n \rightarrow \text{S}_1$ ) and intersystem crossing from excited singlet to excited triplet states

( $S_1 \rightarrow T_1$ ), then, in most of the cases, transfer from these excited states to the accepting electronic levels of  $\text{Ln}^{3+}$  ( $S_1 \rightarrow \text{Ln}^{3+*}$ ,  $T_1 \rightarrow \text{Ln}^{3+*}$ ).<sup>30, 43-44</sup> Other processes such as metal to ligand charge transfer (MLCT) or inter- and intraligand charge transfer (ILCT) states may also play a role in the  $\text{Ln}^{3+}$  sensitization process.<sup>45-50</sup> Another challenge that has to be addressed when creating luminescent  $\text{Ln}^{3+}$ -based coordination compounds is the protection of the  $\text{Ln}^{3+}$  against sources of nonradiative deactivations which are most commonly due to overtones of O-H, N-H, and C-H vibrations.<sup>51</sup> The probability of this process is inversely proportional to the energy gap ( $\Delta E$ ) between the emitting level of the  $\text{Ln}^{3+}$  and the highest energy level of the ground multiplet. Thus,  $\text{Eu}^{3+}$  (12 300  $\text{cm}^{-1}$ ) and  $\text{Tb}^{3+}$  (14 800  $\text{cm}^{-1}$ ), having the largest  $\Delta E$  (not considering UV-emitting  $\text{Gd}^{3+}$ ), exhibit bright red and green emissions in their coordination compounds, and are the most studied and exploited.<sup>52-54</sup> In respect to the NIR emission range,  $\text{Yb}^{3+}$  and  $\text{Nd}^{3+}$  complexes have been mainly considered.<sup>38</sup> Other luminescent  $\text{Ln}^{3+}$ , i.e.  $\text{Pr}^{3+}$ ,  $\text{Sm}^{3+}$ ,  $\text{Dy}^{3+}$ ,  $\text{Ho}^{3+}$ ,  $\text{Er}^{3+}$  and  $\text{Tm}^{3+}$ , usually exhibit less intense emission signals partially because of a smaller  $\Delta E$  or due to the complex electronic structures with several emitting levels.<sup>55</sup> However, these  $\text{Ln}^{3+}$  possess a very unique ability to emit in both the visible and in the NIR ranges.<sup>47, 50, 56</sup> Such dual-emission features of  $\text{Ln}^{3+}$  are less studied and exploited for coordination compounds<sup>57-62</sup> but can lead to, for example, the creation of sophisticated barcode modules<sup>63-66</sup>, or novel optical imaging applications.<sup>67-68</sup>

We have recently reported several series of visible and NIR emitting  $\text{Ln}^{3+}/\text{Ga}^{3+}$  MCs,<sup>5-6, 69</sup> and metallocryptates<sup>70</sup> assembled using salicylhydroxamic acid ( $\text{H}_3\text{shi}$ ) as building blocks. We had demonstrated that  $\text{Ga}^{3+}/\text{shi}$  scaffolds possess a remarkable ability to sensitize the characteristic luminescence of bound visible and NIR-emitting  $\text{Ln}^{3+}$  including the dual-emitting  $\text{Sm}^{3+}$  and  $\text{Dy}^{3+}$ . However, quantitative photophysical properties (i.e. total ( $Q_{\text{Ln}}^{\text{Ln}}$ ) and intrinsic ( $Q_{\text{Ln}}^{\text{Ln}}$ ) quantum yields, observed ( $\tau_{\text{obs}}$ ) and radiative ( $\tau_{\text{rad}}$ ) lifetimes, sensitization efficiencies ( $\eta_{\text{sens}}$ )) have, despite the similarities between the  $\text{Ga}^{3+}/\text{shi}$  based scaffolds, been largely and in many cases unpredictably affected by the nature of the bridging ligands, counter-cations, crystals packing etc.

Herein we present the synthesis, characterization (including X-ray single crystal structural analysis) and detailed photophysical studies of a series of  $\text{Ga}^{3+}/\text{Ln}^{3+}$  MCs with the general composition  $[\text{LnGa}_8(\text{shi})_8(\text{OH})_4]\text{Na}\cdot x\text{CH}_3\text{OH}\cdot y\text{H}_2\text{O}$  (**Ln-1**,  $\text{Ln} = \text{Pr}^{3+}-\text{Yb}^{3+}$ , excluding  $\text{Pm}^{3+}$ ). The  $\text{Y}^{3+}$  analogue was also synthesized to facilitate characterization by  $^1\text{H}$  NMR spectroscopy. Steady-state excitation and emission spectra collected in the visible and/or the NIR ranges,  $Q_{\text{Ln}}^{\text{Ln}}$  and  $\tau_{\text{obs}}$  were measured and analyzed for **Ln-1** in the solid state and, when possible, for solutions in  $\text{CH}_3\text{OH}$  and  $\text{CD}_3\text{OD}$ . The phosphorescence spectrum of **Gd-1** in the solid state was acquired to determine the energy position of the ligand triplet state. More detailed analyses of the photophysical properties, including the determination of  $\tau_{\text{rad}}$ ,  $Q_{\text{Ln}}^{\text{Ln}}$  and  $\eta_{\text{sens}}$ , were performed for **Eu-1** and **Yb-1**.

The presented series of **Ln-1** MCs is remarkable relative to the  $\text{Ga}^{3+}/\text{Ln}^{3+}$  MCs that we have published previously.<sup>3, 5-6, 69</sup> In particular,  $\text{Ln}^{3+}$  in **Ln-1** adopt a pseudo- $D_{4h}$  symmetry compared to  $C_4$  or  $C_1$  symmetries of our previously described MC systems. In addition, **Ln-1** possess a unique ability to sensitize the visible, NIR or dual-emissions of ten  $\text{Ln}^{3+}$  of different natures. The present structure is also the first MC in which efficient sensitization of red  $\text{Eu}^{3+}$  emission occurs. We should note that a  $\text{Ga}^{3+}/\text{Dy}^{3+}$  MC possessing a molecular geometry which shares structural similarities with **Ln-1** but which is formed with another counter-cation ( $\text{nBu}_4\text{N}^+$  vs.  $\text{Na}^+$ ) was obtained through a different synthetic route and was independently reported by the Rentschler group in a recent communication focused exclusively on single molecule magnet properties.<sup>71</sup> Luminescent properties were not described in that publication. It is important to note that we have previously evidenced that the nature of the counter-cation in the MC structure may significantly affect photophysical properties.<sup>69</sup>

## METHODS

*Excitation, emission spectra, observed lifetimes and quantum yields.* Luminescence data were collected for **Ln-1** samples in the solid state or on freshly prepared 50  $\mu\text{M}$  solutions in  $\text{CH}_3\text{OH}$  and  $\text{CD}_3\text{OD}$  placed into 2.4 mm i.d. quartz capillaries or quartz Suprasil cells. Emission and excitation spectra were measured on a Horiba-Jobin-Yvon Fluorolog 3 spectrofluorimeter equipped with either a visible photomultiplier tube (PMT) (220–800 nm, R928P; Hamamatsu), a NIR solid-state InGaAs detector cooled to 77 K (800–1600 nm, DSS-IGA020L; ElectroOptical Systems, Inc., USA), or a NIR PMT (950–1650 nm, H10330-75; Hamamatsu). All spectra were corrected for the instrumental functions. Luminescence lifetimes were determined under excitation at 355 nm provided by a Nd:YAG laser (YG 980; Quantel), the signals in the visible and the NIR ranges were detected with a R928 or H10330-75 PMTs connected to an iHR320 monochromator (Horiba Scientific). The output signals from the detectors were fed into a 500 MHz bandpass digital oscilloscope (TDS 754C; Tektronix) and transferred to a PC for data processing with the Origin 8@ software. Luminescence lifetimes are averages of three or more independent measurements. Quantum yields were determined with a Fluorolog 3 spectrofluorimeter based on the absolute method using an integration sphere (GMP SA, Renens, Switzerland). Each sample was measured several times. The experimental error for the determination of quantum yields is estimated as  $\sim 10\%$ .

*Phosphorescence spectrum.* Phosphorescence spectrum of **Gd-1** in the solid state at 77 K was acquired on a Horiba-Jobin-Yvon Fluorolog 3 spectrofluorimeter in time-resolved mode. See Supporting Information for more details.

*Diffuse reflectance spectra.* For collection of diffuse reflectance spectra **Ln-1** (5 wt.%) were thoroughly grinded with  $\text{MgO}$ . Measurements were performed on a Jasco V670 UV-visible spectrophotometer using a horizontal integration sphere accessory at room temperature.

**Absorption spectra.** Absorption spectra (Figure S9) were collected on freshly prepared 50  $\mu$ M solutions of **Ln-1** in methanol (Merck, Uvasol®) placed in quartz cuvettes on a Jasco V670 UV-visible spectrophotometer in absorbance mode.

**Synthesis and characterization.** All reagents and chemicals were purchased from commercial sources and used without further purification. All reactions were carried out aerobically under ambient conditions. Elemental analysis was performed by Atlantic Microlabs Inc. ESI-MS spectra were collected with an Agilent 6230 TOF HPLC-MS mass spectrometer in negative ion mode (-350V) on samples dissolved in methanol or acetonitrile at a concentration of 2 mg/mL. Single crystals suitable for x-ray analysis were grown via slow evaporation from methanol/water solution at 295 K. See supporting information for x-ray analysis details.

Salicylhydroxamic acid ( $H_3shi$ , 0.4 mmol),  $Ln(NO_3)_3 \cdot xH_2O$  (0.05 mmol,  $Ln^{3+} = Pr^{3+}, Nd^{3+}, Sm^{3+}, Eu^{3+}, Gd^{3+}, Tb^{3+}, Dy^{3+}, Ho^{3+}, Er^{3+}, Tm^{3+}, Yb^{3+}, Y^{3+}$ ), and  $Ga(NO_3)_3 \cdot xH_2O$  (0.4 mmol) were dissolved in 40 mL methanol. Concentrated (~19.8 M) aqueous NaOH solution (1.4 mmol) was added and the solution was stirred overnight. The solution was filtered and the filtrate was left for slow evaporation, producing crystalline compound within 2-3 weeks. Compound was collected via filtration and dried in air. See supporting information for details.

**NMR.** One and two dimensional  $^1H$  NMR were performed on **Y-1** using a Varian VNMRs 500 MHz spectrometer equipped with a Varian 5 mm PFG OneNMR Probe. See supporting information for details.

## RESULTS

### Synthesis and crystal structure of Ln-1

The reaction between  $Ga(NO_3)_3 \cdot xH_2O$ ,  $Ln(NO_3)_3 \cdot xH_2O$  ( $Ln = Pr^{3+}, Nd^{3+}, Sm^{3+}-Yb^{3+}$ ) and salicylhydroxamic acid ( $H_3shi$ ) in a concentrated aqueous sodium hydroxide solution led to the formation of **Ln-1** with the general formula  $[LnGa_8(shi)_8(OH)_4]Na \cdot xCH_3OH \cdot yH_2O$ . Solids were collected as crystalline materials and characterized by ESI mass-spectrometry, elemental analysis, and single crystal unit cell analysis.

X-ray quality crystals of **Nd-1** were grown from the slow evaporation of a methanol solution at ambient temperature. All compounds were found to have identical unit cells confirming the isostructural nature of the compounds (Table S2) allowing a global description of molecular structures of this family of MCs.

The crystal structure of **Nd-1** is depicted in Figure 1d. It was solved in a monoclinic  $P2_1/c$  group. Each molecule contains two  $[12-MC_{Ga^{III}N(shi)-4}]$  units with composition that are identical to the MCs presented previously (Figure 1b, c).<sup>3-5</sup> Each of these MC units is slightly concave in nature and consists of four  $shi^{3-}$  ligands bridging four  $Ga^{3+}$  ions to form a neutral ring. The  $Nd^{3+}$  ion is located in the center of the two MC rings being bound to eight hydroxamate oxygen ions (four from each ring) in a pseudo-square

antiprismatic fashion. Each molecular unit contains a pseudo  $D_{4h}$  symmetry about the  $Nd^{3+}$ . Each of the four MC  $Ga^{3+}$  ions are connected to a counterpart MC  $Ga^{3+}$  ion via a bidentate hydroxide  $[Ga-(\mu_2OH)-Ga]$  bridge. The overall charge of the **Ln-1** MC is -1, balanced by a  $Na^+$  cation.

There are two distinct complex structures present in the crystal of **Nd-1**. The first contains two *C* (clockwise) MC rings of  $[-Ga-N-O-]_4$  motif (when viewed with  $Nd^{3+}$  ion on the opposite side of the ring) binding a single  $Nd^{3+}$ , while the second complex contains two *A* (anti-clockwise) MC rings of  $[-Ga-O-N-]_4$  motif binding a single  $Nd^{3+}$  (Figure S3). The nature of these complexes is consistent with an enantiomeric (non-superimposable mirror-image) relationship between the two isomers such that the above structural description is applicable to both of them. Their physical properties will generally be identical.

Charge neutrality is maintained, and the two isomers are bridged by two  $Na^+$  such that discrete molecular dimers are present in the crystal (Figure S4). Each  $Na^+$  is bound to a phenoxo oxygen and a hydroxamate oxygen belonging to each of the two isomers. Each point of contact is additionally bonded to a  $Ga^{3+}$  ion in a  $[Ga-(\mu_2O)-Na]$  organization. Two oxygens from solvent molecules complete the distorted six-coordinate geometry about the  $Na^+$  ion. Different types of hydrogen bonds formed with solvents of crystallization (water and methanol) can be observed in the structure.

### Behavior of Ln-1 in solution

To assess the behavior of the complexes in solution, mass spectrometry experiments were performed within a timeframe of 10–30 min after preparation of solutions of **Ln-1** in methanol and in acetonitrile. For each  $Ln^{3+}$  analogue in acetonitrile solution, a single large peak with isotopic distribution was identified (except for **Nd-1** and **Pr-1**, for which an additional feature was detected (ESI<sup>+</sup>)), which was consistent with the molecular formula of the monoanion  $[LnGa_8(shi)_8(OH)_4]^-$  ( $[M]^-$ ). This result suggests that the crystalline materials of **Ln-1** are isolated as  $Na[LnGa_8(shi)_8(OH)_4]$ .

For most  $Ln^{3+}$  analogues analyzed by mass spectrometry in methanol solution, the base species  $[M]^-$  were also identified, however, spectra were consistent with the presence of four additional species, i.e.  $[M+14]^-$ ,  $[M+28]^-$ ,  $[M+42]^-$ , and  $[M+56]^-$ . These can be assigned to a sequential replacement of the bridging hydroxide ions ( $OH^-$ ) with methoxide ions ( $CH_3O^-$ ) as in the formula:  $[LnGa_8(shi)_8(OH)_{4-n}(CH_3O)_n]^-$ . This observation is in agreement with the exchange of  $CH_3O^-$  for  $OH^-$  from the gallium(III) ring metals across the entire series of  $Ln^{3+}$  MCs. The short timeline between the solution preparation (maximum 30 min) and the mass spectrometry experiment suggests that  $CH_3O^-/OH^-$  exchange occurs rapidly in methanol solution. Over time  $[LnGa_8(shi)_8(CH_3O)_4]^-$  should become the dominant anion in solution given the prevalence of available  $CH_3O^-$  vs.  $OH^-$  (in a 2 mM solution of **Ln-1** in methanol, the methanol concentration is 24.7 M) although differences in pKa between  $HO^-$  and  $CH_3O^-$  will also be relevant.<sup>72</sup>

To examine the solution stability further, we performed Pulsed Gradient Spin Echo Diffusion Ordered  $^1\text{H}$  NMR Spectroscopy (PGSE DOSY) on a diamagnetic  $\text{Ln}^{3+}$  analogue (**Y-1**) in  $\text{CD}_3\text{OD}$ .<sup>73</sup> NMR signal response to increasing field gradient strength was fit quantitatively to determine experimental diffusion coefficients based on previously described procedures (Table S3).<sup>74-75</sup> In this experiment, it was found that all the identified MC protons migrate together within the time resolution of our experiment. In particular, no protons were found to migrate with a different diffusion coefficient which would be an indication of decomposition, of the MC. Calculations of the diffusion coefficient ( $D$ ) based on the molecular weight and the Stokes-Einstein equation further support the stability of

the MC dimer in solution (Figures S7, S8).<sup>73</sup> For the **Y-1** complex, a  $D$  value of  $4.10 \cdot 10^{-10} \text{ m}^2\text{s}^{-1}$  was calculated. For a hypothetical monomer of **Y-1**, we calculated  $D = 4.54 \cdot 10^{-10} \text{ m}^2\text{s}^{-1}$ . Finally, for a MC dimer with similar ethynylsalicylhydroximate (eshi<sup>3-</sup>) ring ligands but a larger bridging ligand, i.e. isophthalate (iph<sup>-</sup>), and two  $\text{Ln}^{3+}$ ,  $[\text{Ln}_2\text{Ga}_8(\text{eshi})_8(\text{iph})_4]$ , we found  $D = 3.17 \cdot 10^{-10} \text{ m}^2\text{s}^{-1}$ .<sup>76</sup> The experimental  $D$  value for **Y-1**,  $4.23(8) \cdot 10^{-10} \text{ m}^2\text{s}^{-1}$ , is mostly similar to the calculated value for  $\text{NaLnGa}_8(\text{shi})_8(\text{OH})_4$ , and is an intermediate between the values calculated for the monomer and the larger dimer. This suggests that **Y-1** exists in solution as the  $[\text{YGa}_8(\text{shi})_8(\text{OH})_{4-n}(\text{CH}_3\text{O})_n]$  complex in agreement with the crystal structure and mass spectrometry results.

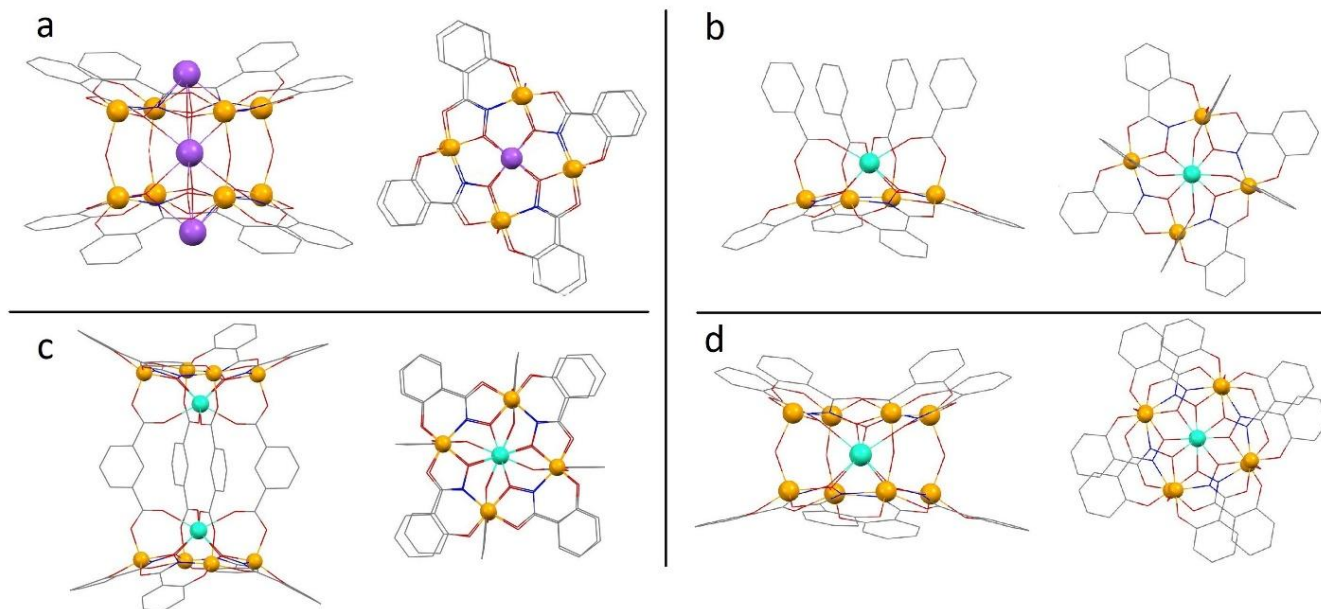


**Figure 1.** Side (left) and top-down (right) views of  $\text{Ga}^{3+}/\text{shi}$  MCs developed by our group. (a)  $[\text{Na}_3\text{Ga}_8(\text{shi})_8(\text{OH})_4]^{4-}$  (b)  $[\text{DyGa}_4(\text{shi})_4(\text{benzoate})_4]^{5-}$  (c)  $[\text{Dy}_2\text{Ga}_8(\text{shi})_8(\text{isophthalate})_4]^{3-}$  (d)  $[\text{NdGa}_8(\text{shi})_8(\text{OH})_4]$ . Solvents of crystallization, non-integral counter ions, and hydrogen atoms have been omitted for clarity. Color code: Ga, orange; Na, violet; Ln, teal; O, red; N, blue; C, grey.

## Photophysical properties

### Ligand-centered photophysical properties

Absorption spectra of **Ln-1** collected in methanol solution (Figure S9) are similar for all the MCs formed with the different lanthanides of and present broad bands in the UV region extending up to 350 nm that are attributed to  $\pi \rightarrow \pi^*$  transitions. Apparent maxima of the lowest in energy absorption bands are located at 313–314 nm and have molar absorption coefficients of  $\sim 3.6 \cdot 10^4 \text{ M}^{-1} \text{ cm}^{-1}$ . The energy of the ligand singlet state ( $S_1$ ) determined from the edge of the absorption spectrum is located at  $28\,690 \text{ cm}^{-1}$  (348.5 nm). Diffuse reflectance spectra of **Ln-1**, similarly to absorption spectra, are dominated by broad-band  $\pi \rightarrow \pi^*$  transitions in the UV range up to 370 nm (Figure S10). Sharp features attributed to f-f transitions have very weak contributions if diffuse reflectance spectra are presented as Kubelka-Munk function vs. wavelength. All of the **Ln-1** complexes exhibit similar diffuse reflectance spectra ex-

cept for **Eu-1** which has a small but distinct extension to the red side of the lowest energy band at  $\sim 375 \text{ nm}$  (Figure S10, right). This difference can likely be attributed to the lower reduction potential of  $\text{Eu}^{3+}/\text{Eu}^{2+}$  in respect to other  $\text{Ln}^{3+}$  and to the formation of a ligand-to-metal charge transfer (LMCT) state.

$\text{Gd}^{3+}$  complexes serve as useful probes to assess the electronic structure of a ligand bound to  $\text{Ln}^{3+}$  due to the  $\text{Gd}^{3+}$  possessing an accepting energy level ( $32\,000 \text{ cm}^{-1}$ )<sup>77</sup> that is too high to be populated by commonly used chromophoric organic ligands. Such complexes are therefore useful to assign ligand triplet ( $T_1$ ) states energies as this state is not depopulated by  $\text{Gd}^{3+}$ . Moreover, its heavy-atom and paramagnetic effects facilitate intersystem crossing<sup>78</sup> and make phosphorescence emission arising from this  $T_1$  state more probable and, in turn, more intense. The energy position of the  $T_1$  level ( $22\,620 \text{ cm}^{-1}$  or 442 nm) was determined as the 0-0 transition from the phospho-

rescence spectrum of the **Gd-1** in the solid state recorded in time-resolved mode at 77 K under 340 nm pulsed excitation after a 200  $\mu$ s delay between excitation and acquisition (Figure S11). The energy diagram reporting the ener-

gy positions measured for the  $S_1$  and the  $T_1$  states in **Gd-1** with respect to the electronic  $\text{Ln}^{3+}$  levels is presented on Figure 2.

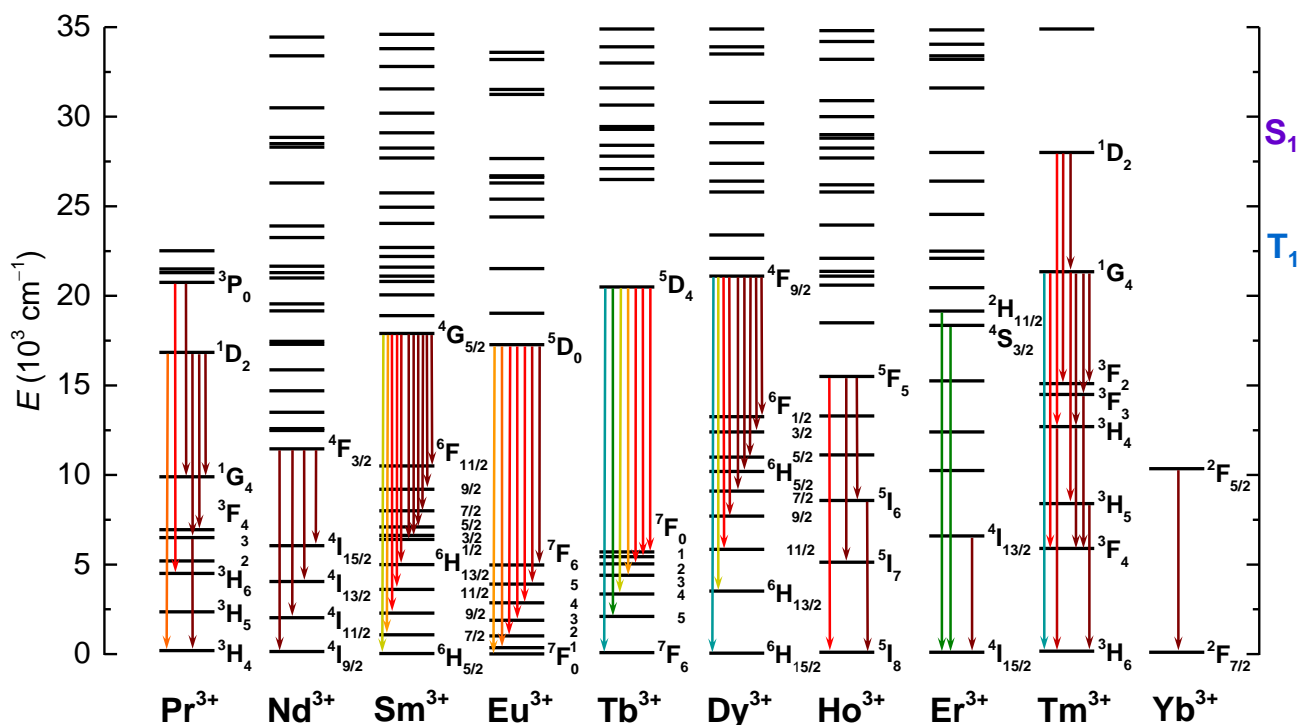


**Figure 2.** Lower energy part of the energy diagram of lanthanide(III) ions emitting in the visible and/or NIR range,<sup>79-81</sup> and energy positions of the ligands singlet ( $S_1$ ) and triplet ( $T_1$ ) states of **Ln-1** MCs. Radiative transitions observed for **Ln-1** MCs are indicated with arrows.

### Lanthanide-centered photophysical properties

Excitation (Figure S12) and emission (Figure 3, S13) spectra,  $\text{Ln}^{3+}$ -centered quantum yields under ligand excitation ( $Q_{\text{Ln}}^{\text{L}}$ ), and observed luminescence lifetimes ( $\tau_{\text{obs}}$ ) (Table 1) were collected for all **Ln-1** ( $\text{Ln} = \text{Pr}^{3+}, \text{Nd}^{3+}, \text{Sm}^{3+}, \text{Eu}^{3+}, \text{Tb}^{3+}-\text{Yb}^{3+}$ ) in the solid state at room temperature. For the sake of comparison,  $Q_{\text{Ln}}^{\text{L}}$  values in Table 1 are reported separately for two ranges of emission wavelengths: 450–800 nm and 800–1650 nm. These are herein referred to as the visible and the NIR emission, respectively. In general, the emission efficiency of lanthanide(III) complexes can be described by the following equation:

$$Q_{\text{Ln}}^{\text{L}} = \eta_{\text{sens}} \cdot Q_{\text{Ln}}^{\text{Ln}} = \eta_{\text{sens}} \cdot \frac{\tau_{\text{obs}}}{\tau_{\text{rad}}} \quad (1)$$

where  $\eta_{\text{sens}}$  is the sensitization efficiency of the organic ligands that takes into account the energy migration pro-

cesses occurring both within the ligands and from the ligand to the  $\text{Ln}^{3+}$  excited state;  $Q_{\text{Ln}}^{\text{Ln}}$  is the intrinsic quantum yield or quantum yield upon direct f-f excitation, it reflects the relative importance of radiative and non-radiative processes within  $\text{Ln}^{3+}$ ;  $\tau_{\text{rad}}$  is the radiative lifetime, or the lifetime in absence of non-radiative deactivation processes.  $Q_{\text{Ln}}^{\text{Ln}}$  is usually difficult to measure directly because of the very weak absorption of f-f transitions, however, it can be estimated as a ratio of  $\tau_{\text{rad}}$  and the observed lifetimes ( $\tau_{\text{obs}}$ ).<sup>43, 82</sup> The latter parameter is routinely accessed experimentally but the determination of  $\tau_{\text{rad}}$  is less straightforward.<sup>83</sup> Presently, we estimated  $\tau_{\text{rad}}$  for **Yb-1** using its absorption spectrum (Supporting Information, Figure S19), and for **Eu-1** using its emission spectrum (*vide infra*).

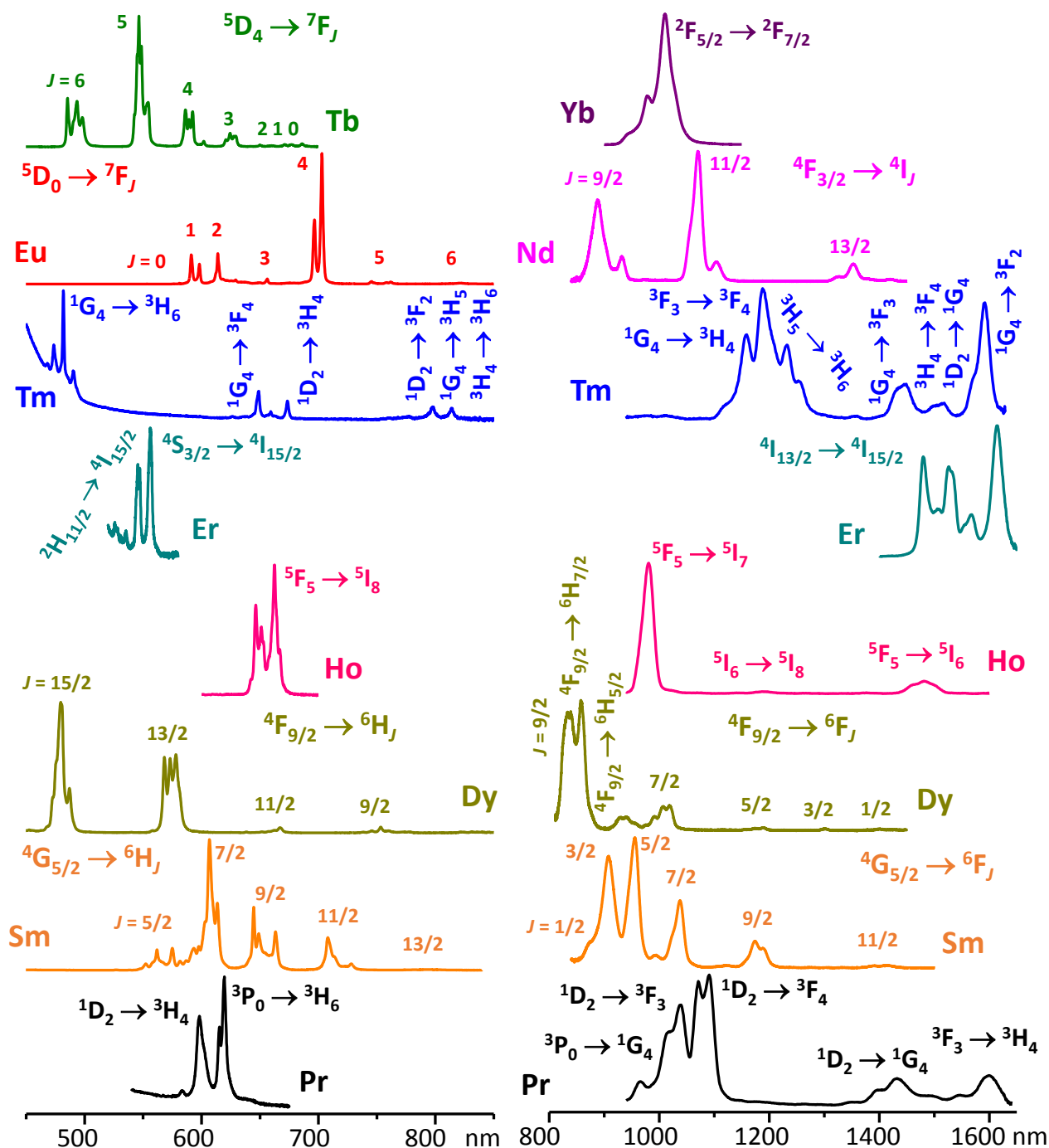


**Figure 3.** Highlights of the Ln<sup>3+</sup>-centered emission signals of Ln-1 MCs in the solid state under excitation at 340 nm at room temperature. Intensities of the emission spectra are normalized to the corresponding intensity maxima located in the range 450-850 nm (left) or 800-1650 nm (right).

To further establish the relationship between structure and luminescence properties, a high-resolution emission spectrum was acquired for Eu-1 in the solid state (Figure S17, S18). To get information about the behavior of the studied MCs in solution and to assess the number of solvent molecules potentially coordinated to the Ln<sup>3+</sup> (Supporting Information), a series of measurements was performed on solutions of selected Ln-1 (Ln = Nd<sup>3+</sup>, Sm<sup>3+</sup>, Eu<sup>3+</sup>, Tb<sup>3+</sup>, Dy<sup>3+</sup>, Yb<sup>3+</sup>) in CH<sub>3</sub>OH and CD<sub>3</sub>OD (Table 1, Figure 4,

S14, S15). For the less luminescent Ln-1 (Ln = Pr<sup>3+</sup>, Ho<sup>3+</sup>, Er<sup>3+</sup>, Tm<sup>3+</sup>), excitation and emission spectra were only collected in CD<sub>3</sub>OD (Figure S16). The assignment of the bands in the excitation and emission spectra was done according to existing literature.<sup>79-81, 84-85</sup>

Excitation spectra collected for Ln-1 in the solid state upon monitoring the main emission bands of the corresponding Ln<sup>3+</sup> in the visible and/or the NIR ranges are dominated by broad ligand-centered bands in the UV up to

375 nm on the lower energy side, or 425 nm in the case of Eu-1 (Figure S12). The extension of the excitation band to the red for Eu-1 is in line with the diffuse reflectance spectrum (Figure S10, right) and the formation of LMCT state for this MC (*vide supra*) by describing the same electronic structure of the ligand-Eu<sup>3+</sup> interaction. In addition to the broad bands present in the excitation spectra of all **Ln-1** (except **Yb-1**) sharper features that correspond to f-f transitions that are specific to the nature of the specific Ln<sup>3+</sup> are observed. These bands have different relative intensities compared to the ligand-centered ones and vary between the particular Ln<sup>3+</sup> of interest. For example, direct f-f excitation bands are almost inconsequential in the case of **Tb-1** while reaching 75% of the intensity of the ligand

maximum signal for **Nd-1**. Excitation spectra of **Ln-1** measured in methanol solutions matches the absorption spectra and present only broad bands in the UV up to 350 nm. Expanded excitation range for solid state samples compared to those in solution can be explained by saturation effects.<sup>86-87</sup> All these observations reflect the ability of the MC scaffold in **Ln-1** to sensitize characteristic visible and NIR emissions of several Ln<sup>3+</sup> of different natures through a common electronic structure.

Indeed, upon excitation into ligand-centered bands at 340 or 310 nm for samples in the solid state or in solution, respectively, **Ln-1** exhibit sharp emission bands in the visible and/or NIR ranges that are specific to the corresponding f-f transitions (Figure 3, S13, S15, S16).

**Table 1. Luminescence lifetimes ( $\tau_{\text{obs}}$ ) and Ln<sup>3+</sup>-centered quantum yields collected under ligand excitation ( $Q_{\text{Ln}}^{\text{L}}$ ) for **Ln-1**.<sup>a</sup>**

Ln	State/ Solvent	$\tau_{\text{obs}}$ ( $\mu\text{s}$ ) <sup>b</sup>	Level/ wavelength (nm) <sup>c</sup>	$Q_{\text{Ln}}^{\text{L}}$ (%) <sup>d</sup>	
				450–800 nm	800–1650 nm
Pr	Solid	0.101(2)	<sup>1</sup> D <sub>2</sub> / 1090	3.0(2)·10 <sup>-2</sup>	4.91(6)·10 <sup>-3</sup>
Nd	Solid	0.91(1)	<sup>4</sup> F <sub>3/2</sub> / 1070		0.30(2)
	CH <sub>3</sub> OH	1.09(3) : 91(2)% ; 0.34(3) : 9(2)%	"		0.167(4)
	CD <sub>3</sub> OD	5.9(1) : 89 (2)% ; 2.0(2) : 10(2)%	"		0.90(2)
Sm	Solid	151(1)	<sup>4</sup> G <sub>5/2</sub> / 611	10.4(6)	0.193(2)
	CH <sub>3</sub> OH	83.4(3)	"	10.1(5)	7.98(3)·10 <sup>-2</sup>
	CD <sub>3</sub> OD	721(3)	"	83(1)	0.71(2)
Eu	Solid	1360(10)	<sup>5</sup> D <sub>0</sub> / 705	4.16(6)	
	CH <sub>3</sub> OH	1950(1)	"	15.4(1)	
	CD <sub>3</sub> OD	2500(10)	"	21(1)	
Tb	Solid	1040(50): 87(1)% ; 390(30): 13(1)%	<sup>5</sup> D <sub>4</sub> / 545	35(2)	
	CH <sub>3</sub> OH	1870(10)	"	47.7(2)	
	CD <sub>3</sub> OD	1950(10)	"	50.8(9)	
Dy	Solid	37.7(8): 55(1)% ; 4.1(1): 45(1)%	<sup>4</sup> F <sub>9/2</sub> / 577	1.26(7)	3.09(9)·10 <sup>-2</sup>
	CH <sub>3</sub> OH	24.8(2) : 87(1)% ; 2.69(9) : 13(1)%	"	6.9(3)	5.0(2)·10 <sup>-2</sup>
	CD <sub>3</sub> OD	41.5(8) : 92(1)% ; 4.54(7) : 8(1)%	"	9.46(6)	7.7(4)·10 <sup>-2</sup>
Ho	Solid	0.0385(9)	<sup>5</sup> F <sub>5</sub> / 980	2.20(8)·10 <sup>-2</sup>	2.9(3)·10 <sup>-3</sup>
Er	Solid	1.93(6)	<sup>4</sup> I <sub>13/2</sub> / 1525	<sup>e</sup>	1.90(4)·10 <sup>-2</sup>
Tm	Solid	1.37(1)	<sup>1</sup> G <sub>4</sub> / 482	5.8(2)·10 <sup>-2</sup>	4.7(2)·10 <sup>-5</sup>
Yb	Solid	27.4(9)	<sup>2</sup> F <sub>5/2</sub> / 1010		2.8(1)
	CH <sub>3</sub> OH	15.6(2)	"		0.78(4)
	CD <sub>3</sub> OD	196(1)	"		8.4(1)

<sup>a</sup> For samples in the solid state or for 50  $\mu\text{M}$  solutions in CH<sub>3</sub>OH or CD<sub>3</sub>OD, at room temperature, 2 $\sigma$  values between parentheses. Estimated experimental errors:  $\tau_{\text{obs}}$ ,  $\pm 2\%$ ;  $Q_{\text{Ln}}^{\text{L}}$ ,  $\pm 10\%$ . <sup>b</sup> Under excitation at 355 nm. If a biexponential decay was observed, popu-

lation parameters  $P_i = \frac{B_i \tau_i}{\sum_{i=1}^n B_i \tau_i}$  in % are given after the colon. <sup>c</sup> Main emitting level and the corresponding wavelength used to record luminescence decays. <sup>d</sup> Under excitation at 340 nm for the samples in the solid state and at 310 nm for solutions. <sup>e</sup> Too low to be determined.

**Pr-1** in the solid state exhibits both visible and NIR emission bands arising mainly from  $^1D_2$ , but also from  $^3P_0$  and  $^3F_3$  excited states levels. Two visible emission bands are present in the range of 570–660 nm and are assigned to the  $^1D_2 \rightarrow ^3H_4$  and  $^3P_0 \rightarrow ^3H_6$  transitions with a  $Q_{Pr}^L$  value of  $3.0 \cdot 10^{-2}\%$ . In the NIR domain, emission bands arise from the  $^3P_0 \rightarrow ^1G_4$ ,  $^1D_2 \rightarrow ^3F_3$ ,  $^3F_4$ ,  $^1G_4$ , and  $^3F_3 \rightarrow ^3H_4$  electronic transitions and are observed in the range 950–1650 nm.  $Q_{Pr}^L$  (NIR) was found to be  $4.9 \cdot 10^{-3}\%$ , while the  $\tau_{obs}$  value of the  $^1D_2$  level is 101(2) ns. NIR emission of weaker intensity of **Pr-1** could be detected in CD<sub>3</sub>OD solution (Figure S16).

**Nd-1** in the solid state, solutions in CH<sub>3</sub>OH and CD<sub>3</sub>OD shows NIR luminescence in the range of 850–1450 nm with three main bands at ~885, 1065 and 1350 nm due to the  $^4F_{3/2} \rightarrow ^4I_J$  ( $J = 9/2-13/2$ ) transitions. The general features of each of them remain similar for the sample in the solid state and in the solution. However, the relative intensity of the emission band corresponding to the  $^4F_{3/2} \rightarrow ^4I_{9/2}$  transition significantly increases for the latter. Luminescence decays are monoexponential for the solid state sample and are biexponential in solution, with the 10% contribution of a short-lived component.  $\tau_{obs}$  values are comparable for the solid state sample and in solution in CH<sub>3</sub>OH while  $Q_{Nd}^L$  is decreased from 0.3 to 0.17%. In CD<sub>3</sub>OD solution, both  $\tau_{obs}$  and  $Q_{Nd}^L$  are significantly increased reaching values of 5.9  $\mu$ s and 0.9%, respectively.

**Sm-1** emits in both visible and NIR, emission signals arising from the  $^4G_{5/2}$  level in the solid state and solutions. Multiple sharp emission bands in the visible range can be assigned to  $^4G_{5/2} \rightarrow ^3H_J$  ( $J = 5/2-13/2$ ) transitions with  $^4G_{5/2} \rightarrow ^3H_{7/2}$  dominating the spectrum and being responsible for the pink-orange color of Sm-1 emission. NIR emission is derived from  $^4G_{5/2} \rightarrow ^6F_J$  ( $J = 5/2-13/2$ ) transitions. The crystal-field splitting of the emission bands is very similar for the **Sm-1** in the solid state and in solution but the relative intensities of the  $^4G_{5/2} \rightarrow ^3H_{9/2, 11/2}$ ,  $^6F_{7/2, 9/2}$  transitions are smaller for the latter. A residual broad-band ligand-centered emission is observed at wavelengths <450 nm. Quantitative data are provided in Table S6. The values of  $Q_{Sm}^L$  (visible) are essentially the same (~10%) for the sample in the solid state and in the CH<sub>3</sub>OH solution, while  $\tau_{obs}$  are 1.8-times shorter for the latter. Both parameters are drastically enhanced in CD<sub>3</sub>OD solution reaching 83% and 721  $\mu$ s. The values of  $Q_{Sm}^L$  in the NIR are lower and increase in the following order: CH<sub>3</sub>OH < solid state < CD<sub>3</sub>OD.

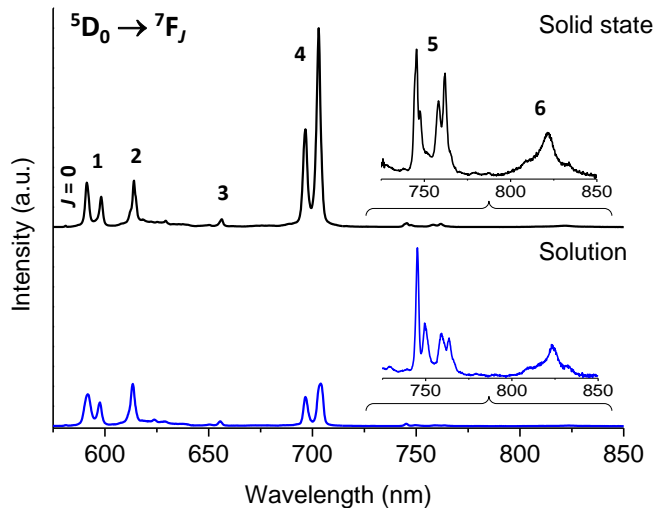


**Figure 4.** Comparison between emission spectra for **Eu-1** in the solid state ( $\lambda_{ex} = 340$  nm) and in the 50  $\mu$ M methanol solution ( $\lambda_{ex} = 310$  nm) at room temperature (emission bandpass 1 nm, acquisition increment 0.2 nm). The spectra have been scaled so that the respective  $^5D_0 \rightarrow ^7F_1$  transitions have identical integrated areas.

**Eu-1** shows red luminescence with sharp emission bands assigned to  $^5D_0 \rightarrow ^7F_J$  ( $J = 0-6$ ) transitions (Figure 4). The strictly forbidden  $^5D_0 \rightarrow ^7F_0$  transition results in an emission band possessing very low intensity. However, all the other transitions including the rarely observed  $^5D_0 \rightarrow ^7F_{5,6}$  can be clearly distinguished. In the solid state, the **Eu-1** emission spectrum is dominated by the  $^5D_0 \rightarrow ^7F_4$  transition that has 60.9% contribution to the total emission intensity (Table S4). The hypersensitive  $^5D_0 \rightarrow ^7F_2$  and magnetic dipole  $^5D_0 \rightarrow ^7F_1$  transitions have almost equal contribution with the ratio  $I(^5D_0 \rightarrow ^7F_2)/I(^5D_0 \rightarrow ^7F_1)$  equal to 1.25. Such observations are consistent with a square antiprismatic environment around Eu<sup>3+</sup> and a pseudo- $D_{4h}$  symmetry (*vide supra*).<sup>88</sup> At room temperature  $Q_{Eu}^L$  is equal to 4.2 % while  $\tau_{obs}$  is almost temperature independent (1.36 ms at 298K vs. 1.55 ms 10K).

To gain more insight about Eu<sup>3+</sup> environment, a high-resolution emission spectrum of **Eu-1** in the solid state was recorded at 10K (Figure S18). The narrow  $^5D_0 \rightarrow ^7F_0$  transition has a full-width at half-maximum (FWHM) of 10 cm<sup>-1</sup> and a maximum at 17 209 cm<sup>-1</sup> (Figure S17). The observation of a single emission band for this transition reflects the presence of only one type of emitting Eu<sup>3+</sup> species in **Eu-1** and therefore of a unique environment around this metal ion. In addition, it is generally accepted that the energy of the  $^5D_0 \rightarrow ^7F_0$  transition ( $\tilde{\nu}$ ) and, in particular, its shift from the energy determined for Eu<sup>3+</sup> in the gas phase ( $\tilde{\nu}_0 = 17\,374$  cm<sup>-1</sup>) depends on the nephelauxetic effect generated by the coordinating ligands. Several ap-

proaches have been suggested to estimate this effect,<sup>89</sup> but if considering the one by Frey and Horrocks:<sup>90</sup>

$$\tilde{\nu} = \tilde{\nu}_0 + C_{CN} \sum_{i=1}^{CN} n_i \delta_i \quad (2)$$

where  $\delta_i$  is the nephelauxetic parameter for each coordinating ligand or group,  $n_i$  is the index of such groups, CN is the coordination number (CN = 8 for **Eu-1**), and  $C_{CN}$  is a coefficient that depends on CN ( $C_{CN} = 1.06$  for CN = 8). If taking into account an approximation that  $\tilde{\nu}$  increase by 1  $\text{cm}^{-1}$  when the temperature rises by 24 K,  $\tilde{\nu}$  equals to 17 221  $\text{cm}^{-1}$  at 298K. Therefore,  $\delta_i = -18$  for the shi<sup>3-</sup> ligand's binding hydroximate oxygens, a value which is close to the effect induced by a charged carboxylate oxygen ( $\delta_i = -18.2$ ).<sup>90</sup> The  $^5\text{D}_0 \rightarrow ^7\text{F}_1$  transition contains two-fold degenerate and non-degenerate components that correspond to  $^7\text{F}_1$  crystal-field sublevels located at 285.1, 335.3 and 506.2  $\text{cm}^{-1}$  above the  $^7\text{F}_0$  level. Such splitting reflects a pseudo-tetragonal symmetry around  $\text{Eu}^{3+}$  consistent with the square antiprism coordination environment.

The crystal-field splitting of  $^5\text{D}_0 \rightarrow ^7\text{F}_j$  ( $J = 0-6$ ) transitions in the emission spectrum of **Eu-1** in methanol solution are very similar to those observed in the solid state (Figure 4). However, the contribution of the  $^5\text{D}_0 \rightarrow ^7\text{F}_4$  transition to the total emission intensity is decreased to 34.1% (vs. 60.9% in the solid state). On the other hand, the ratio  $I(^5\text{D}_0 \rightarrow ^7\text{F}_2)/I(^5\text{D}_0 \rightarrow ^7\text{F}_1)$  remains comparable (1.18 vs. 1.25) (Table S4). Compared to the solid state sample, the values of  $\tau_{\text{obs}}$  and  $Q_{\text{Eu}}^{\text{L}}$  increase by 1.4 and 3.7 times, respectively, for **Eu-1** in  $\text{CH}_3\text{OH}$  solution. In deuterated solvent, these parameters increase by 1.8 and 5.0 fold respectively (Table 2).

To get more information about the parameters that affect the **Eu-1** emission intensity,  $\tau_{\text{rad}}$  and the corresponding  $Q_{\text{Eu}}^{\text{Eu}}$  and  $\eta_{\text{sens}}$  were estimated using eq. 1 (Table 2). In the case of  $\text{Eu}^{3+}$ , the  $^5\text{D}_0 \rightarrow ^7\text{F}_1$  transition has a purely magnetic dipolar character, is insensitive to the  $\text{Eu}^{3+}$  coordination environment and, when  $J$ -mixing is considered to be small, the integrated intensity of the  $^5\text{D}_0 \rightarrow ^7\text{F}_1$  transition ( $I_{\text{MD}}$ ) can be used to calibrate the total integrated emission intensity arising from  $^5\text{D}_0 \rightarrow ^7\text{F}_j$  ( $J = 0-6$ ) transitions ( $I_{\text{tot}}$ ) and to determine  $\tau_{\text{rad}}$  via the equation:<sup>82, 91</sup>

$$\frac{1}{\tau_{\text{rad}}} = A_{\text{MD},0} \cdot n^3 \left( \frac{I_{\text{tot}}}{I_{\text{MD}}} \right) \quad (3)$$

where  $A_{\text{MD},0}$  is the spontaneous emission probability of the  $^5\text{D}_0 \rightarrow ^7\text{F}_1$  transition being equal to 14.65  $\text{s}^{-1}$ ,  $n$  is the refractive index.  $\tau_{\text{rad}}$  are 2.8 fold longer for **Eu-1** in solution compared to those recorded in the solid state, leading to a 1.5-2 times decrease of the intrinsic quantum yields. On the other hand, the 7.3 fold increased sensitization efficiency of the ligands in solutions results in an overall increase of  $Q_{\text{Eu}}^{\text{L}}$ .

**Table 2. Photophysical parameters obtained for Eu-1 in the solid state and in 50  $\mu\text{M}$  solutions.<sup>a</sup>**

State/ Solvent	$\tau_{\text{obs}}$ (ms)	$\tau_{\text{rad}}$ (ms) <sup>b</sup>	$Q_{\text{Eu}}^{\text{Eu}}$ (%)	$Q_{\text{Eu}}^{\text{L}}$ (%)	$\eta_{\text{sens}}$ (%)
Solid state	1.36(1)	2.78	49	4.16(6)	8.5
$\text{CH}_3\text{OH}$	1.95(1)	7.80	24	15.4(5)	62
$\text{CD}_3\text{OD}$	2.50(1)	7.87	32	21(1)	66

<sup>a</sup> At room temperature,  $2\sigma$  values between parentheses. Relative errors:  $\tau_{\text{obs}}$ ,  $\pm 2\%$ ;  $Q_{\text{Eu}}^{\text{L}}$ ,  $\pm 10\%$ ;  $\tau_{\text{rad}}$ ,  $\pm 10\%$ ;  $Q_{\text{Eu}}^{\text{Eu}}$ ,  $\pm 12\%$ ;  $\eta_{\text{sens}}$ ,  $\pm 22\%$ . <sup>b</sup> Calculated using Eq. 3 according to ref. <sup>91</sup>;  $n(\text{solid state}) = 1.5$ ;  $n(\text{CH}_3\text{OH}) = 1.33$ ;  $n(\text{CD}_3\text{OD}) = 1.326$ .

**Tb-1** in the solid state and in solution exhibits a bright green emission arising from  $^5\text{D}_4 \rightarrow ^7\text{F}_j$  ( $J = 6-0$ ) transitions with  $Q_{\text{Tb}}^{\text{L}}$  of 35–51%. The crystal field splitting of the  $^5\text{D}_4 \rightarrow ^7\text{F}_j$  bands is similar for **Tb-1** in the solid state and in solution (Figure S14). On the other hand, the relative integral intensity of the  $^5\text{D}_4 \rightarrow ^7\text{F}_6$  transition increases by 1.5 fold while for the other  $^5\text{D}_4 \rightarrow ^7\text{F}_j$  ( $J = 4-0$ ) transitions a diminution by 1.4–3 fold is observed (Table S5). Experimental luminescence decays arising from the  $^5\text{D}_4$  level in the solid state are best fitted with a biexponential function with the dominating contribution (87 %) from the long component (1040  $\mu\text{s}$ ) and an average  $\tau_{\text{obs}}$  value of 1010  $\mu\text{s}$ .  $\tau_{\text{obs}}$  measured at 10 K were found to be  $\tau_1 = 1040(10)$   $\mu\text{s}$  ( $P_1 = 96.4(4)$  %) and  $\tau_2 = 272(5)$   $\mu\text{s}$  ( $P_2 = 3.6(4)$  %) giving an average value of 1030  $\mu\text{s}$ . The similarity of the average values of  $\tau_{\text{obs}}$  when going from 298 K to 10 K reflects the absence or an insignificant role of temperature dependent non-radiative processes including Boltzmann dependent back energy transfer in **Tb-1**. Luminescence decays of **Tb-1** in solution are monoexponential and the corresponding  $\tau_{\text{obs}}$  values are  $\sim 2.2$  times longer than those recorded in the solid state.

**Dy-1** in the solid state and in solution emits both visible and NIR light originating from the  $^4\text{F}_{9/2}$  level.<sup>85</sup> In the visible regime, the emission spectrum is dominated by the  $^4\text{F}_{9/2} \rightarrow ^6\text{H}_{15/2}$  transition centered at 480 nm, while in the NIR region the emission is dominated by the bands associated with the  $^4\text{F}_{9/2} \rightarrow ^6\text{H}_{9/2, 7/2}$  transitions in the range of 800–880 nm. A residual broad-band ligand-centered emission <450 nm is observed (Figure S14, Table S6). The values of  $Q_{\text{Dy}}^{\text{L}}$  (visible) of **Dy-1** in  $\text{CH}_3\text{OH}$  and  $\text{CD}_3\text{OD}$  are 5.5 and 7.5 times higher than in the solid state.  $\text{Dy}^{3+}$ -centered emission in the NIR is also enhanced in solution compared to the solid state but to a lesser extent, by a 1.6–2.5 fold. Luminescence decays curves recorded at 298 K upon monitoring the emission from the  $^4\text{F}_{9/2}$  level are biexponential with an almost equal contribution from the short and the long components, and the average value of 35  $\mu\text{s}$ . At 10 K, the latter value is 3.5 times longer (123  $\mu\text{s}$ ) in respect to  $\tau_1 = 125(1)$   $\mu\text{s}$  ( $P_1 = 92.7(6)\%$ ) and  $\tau_2 = 35(1)$   $\mu\text{s}$  ( $P_2 = 7.3(6)\%$ ). Such behavior can be explained by the existence of the temperature-dependent non-radiative energy transfer processes such as the back transfer from the  $\text{Dy}^{3+} ^4\text{F}_{9/2}$  level (21 100  $\text{cm}^{-1}$ )<sup>81</sup> to the closely located triplet state of the ligands (22 620  $\text{cm}^{-1}$ ). In contrast to the behavior of **Tb-1**, **Dy-1** luminescence decays in solutions remain biexponential, although the contribution of the longer component is increased to 87–92 % vs. 55 % for the solid state. The average  $\tau_{\text{obs}}$  values are similar for the solid state

sample and the solution in CH<sub>3</sub>OH (19.1  $\mu$ s and 21.1  $\mu$ s) but they increase to 37.9  $\mu$ s for the CD<sub>3</sub>OD solution.

**Ho-1** in the solid state exhibits both visible and NIR emissions. The visible emission in the range of 635–680 nm is attributed to the  $^5F_5 \rightarrow ^5I_8$  transition and has a  $Q_{\text{Ho}}^{\text{L}}$  (visible) of  $2.20(8) \cdot 10^{-2}$  %. NIR emission signal is dominated by the  $^5F_5 \rightarrow ^5I_7$  transition at 980 nm with smaller contributions from the  $^5F_5 \rightarrow ^5I_6$  band at 1480 nm and a faint participation of the  $^5I_6 \rightarrow ^5I_8$  transition at 1190 nm. The observed luminescence lifetime of the  $^5F_5$  level is 38.5(9) ns.

**Er-1** in the solid state shows multiple emission bands located in the range 1450–1650 nm and assigned to the  $^4I_{13/2} \rightarrow ^4I_{15/2}$  transition. The luminescence decay of the  $^4I_{13/2}$  level is monoexponential with a  $\tau_{\text{obs}}$  value of 1.93(6)  $\mu$ s.  $Q_{\text{Er}}^{\text{L}}$  (NIR) is equal to  $1.90(4) \cdot 10^{-2}$  %. In addition to the NIR emission, faint Er<sup>3+</sup> transitions in the visible range between 520 and 565 nm due to  $^2H_{11/2} \rightarrow ^4I_{15/2}$  and  $^4S_{3/2} \rightarrow ^4I_{15/2}$  transitions were detected, however quantitative parameters related to these bands could not be determined.

**Tm-1** possesses faint visible and NIR emissions with multiple bands arising from the  $^1G_4$ ,  $^1D_2$ ,  $^3H_4$  and  $^3F_3$  excited levels.<sup>84</sup> In the visible range, the  $^1G_4 \rightarrow ^3H_6$  transition with a maximum at 480 nm overlaps with the broad ligand-centered emission (Figure S13). Other bands are observed in the range of 620–840 nm. The total  $Q_{\text{Tm}}^{\text{L}}$  (visible) equal to  $5.8(2) \cdot 10^{-2}$  % and the  $\tau_{\text{obs}}$  of the  $^1G_4$  level is 1.37(1)  $\mu$ s. Moreover, Tm<sup>3+</sup> f-f specific electronic transitions with maxima at 1188, 1448 and 1592 nm could be detected in the range of 1100–1650 nm with  $Q_{\text{Tm}}^{\text{L}}$  (NIR) of  $4.7(2) \cdot 10^{-5}$  %.

**Yb-1** in the solid state and solutions displays NIR emission in the range of 920–1100 nm with a maximum at 1010 nm arising from the  $^2F_{5/2} \rightarrow ^2F_{7/2}$  transition. The values of  $\tau_{\text{obs}}$  and  $Q_{\text{Yb}}^{\text{L}}$  decrease by 1.8 and 3.6 times, respectively, when comparing **Yb-1** in the solid state and in CH<sub>3</sub>OH solution. In deuterated methanol, both values are significantly enhanced, reaching 196  $\mu$ s and 8.4 %. To get additional information about the different parameters that impact the global **Yb-1** emission efficiency,  $\tau_{\text{rad}}$  was estimated from the absorption spectrum measured in the range of the  $^2F_{5/2} \leftarrow ^2F_{7/2}$  transition (Figure S19) using the modified Einstein’s equation (Supporting Information).<sup>91</sup> The data are provided in Table 3 together with the values reported previously for other Yb<sup>3+</sup>/Ga<sup>3+</sup> MCs for comparison.

**Table 3. Photophysical parameters obtained for Yb-1 in solution and comparison with other Yb<sup>III</sup>/Ga<sup>III</sup> MCs.<sup>a</sup>**

MC	Solvent	$\tau_{\text{obs}}$ ( $\mu$ s)	$\tau_{\text{rad}}$ ( $\mu$ s) <sup>b</sup>	$Q_{\text{Yb}}^{\text{Yb}}$ (%)	$Q_{\text{Yb}}^{\text{L}}$ (%)	$\eta_{\text{sens}}$ (%)
Yb-1	CH <sub>3</sub> OH	15.6(2)	814	1.9	0.78(4)	41
	CD <sub>3</sub> OD	196(1)	819	24	8.4(1)	35
YbGa <sub>4</sub> (1) <sup>c</sup>	CH <sub>3</sub> OH	2.06(4)	530	0.39	0.26(1)	67

	CD <sub>3</sub> OD	36.6(1)	530	6.9	4.29(1)	62
YbGa <sub>4</sub> (2) <sup>d</sup>	CH <sub>3</sub> OH	1.72(1)	590	0.29	0.123(2)	42
	CD <sub>3</sub> OD	27.4(1)	590	4.6	2.55(5)	55

<sup>a</sup> At room temperature, 2 $\sigma$  values between parentheses. Relative errors:  $\tau_{\text{obs}}$ ,  $\pm 2\%$ ;  $Q_{\text{Yb}}^{\text{L}}$ ,  $\pm 10\%$ ;  $\tau_{\text{rad}}$ ,  $\pm 10\%$ ;  $Q_{\text{Yb}}^{\text{Yb}}$ ,  $\pm 12\%$ ;  $\eta_{\text{sens}}$ ,  $\pm 22\%$ . <sup>b</sup> See Supporting Information for details; for CD<sub>3</sub>OD solutions recalculated taking into account the refractive index  $n(\text{CD}_3\text{OD}) = 1.326$ . <sup>c</sup> [YbGa<sub>4</sub>(shi)<sub>4</sub>(benzoate)<sub>4</sub>] from Ref.<sup>5</sup> <sup>d</sup> [YbGa<sub>4</sub>(shi)<sub>4</sub>(H<sub>2</sub>shi)<sub>2</sub>] from Ref.<sup>6</sup>

## DISCUSSION

### Synthesis and characterization

**Ln-1** is the direct Ln<sup>3+</sup>-centered analogue of the [Na<sub>3</sub>Ga<sub>8</sub>(shi)<sub>8</sub>(OH)<sub>4</sub>] structure published previously by our group (Figure 1a).<sup>4</sup> It is also a major evolution of the Ga<sup>3+</sup>/Ln<sup>3+</sup> luminescent MCs created by us initially with the monomeric [LnGa<sub>4</sub>(shi)<sub>4</sub>(benzoate)<sub>4</sub>] (Figure 1b),<sup>5</sup> then with the [Ln<sub>2</sub>Ga<sub>8</sub>(shi)<sub>8</sub>(isophthalate)<sub>4</sub>] (Figure 1c)<sup>3</sup> series. The [LnGa<sub>8</sub>(shi)<sub>8</sub>(OH)<sub>4</sub>] MC (Figure 1d) possesses a pseudo-*D*<sub>4h</sub> symmetry about the central Ln<sup>3+</sup> as compared to the previously mentioned Ga<sup>3+</sup>/Ln<sup>3+</sup> MCs in which the Ln<sup>3+</sup> is located on a pseudo-*C*<sub>4</sub> axis of symmetry.

The ESI-MS mass-spectra of **Ln-1** measured in acetonitrile and methanol solutions revealed the exclusive presence of the MC species. The DOSY NMR data performed on **Y-1** further supports this observation (Supporting Information). Together, these results suggest that the **Ln-1** MCs are present as stable dimers in solution. However, in methanol solution, as indicated by mass spectrometry experiments, a rapid OH<sup>−</sup>/CH<sub>3</sub>O<sup>−</sup> exchange occurs which will eventually lead to CH<sub>3</sub>O<sup>−</sup> becoming the dominant bridging ion and [LnGa<sub>8</sub>(shi)<sub>8</sub>(CH<sub>3</sub>O)<sub>4</sub>] becoming the main species.

### Photophysical properties

In the solid state, upon excitation into the ligand-centered bands at 340 nm, **Eu-1** and **Tb-1** exhibit bright red and green emission signals while **Yb-1** and **Nd-1** show their respective characteristic transitions in the NIR range (Figure 3). For **Pr-1**, **Sm-1**, **Dy-1**, **Ho-1**, **Er-1** and **Tm-1** dual-range emissions with bands located in the visible and in the NIR ranges were detected. It should be noted such observation of dual emission for six Ln<sup>3+</sup> using one type of molecular compound are very scarce.<sup>47, 50, 56, 62, 92</sup> Additionally, if the dual emission of Sm<sup>3+</sup> and Dy<sup>3+</sup> are more frequently observed and quantified,<sup>3, 5-6, 46-47, 57, 60, 65, 67-68, 85, 93-94</sup> studies that involve evaluation of such properties from Pr<sup>3+</sup>, Ho<sup>3+</sup>, Er<sup>3+</sup> and Tm<sup>3+</sup> in coordination compounds are very rare.<sup>58-59, 61, 64, 95</sup> However, unique bands arising from Ln<sup>3+</sup> of different natures and spanning the whole visible and NIR ranges with various luminescence lifetimes and emission profiles are essential for multicolor and multiplex imaging,<sup>96-97</sup> and could lead to the development of advanced materials such as sophisticated barcode modules<sup>63-65</sup> or other interesting optical imaging applications.<sup>67-68</sup>

It is generally accepted that the lowest in energy triplet state of chromophoric ligands play a predominant role in the sensitization of  $\text{Ln}^{3+}$  although singlet and charge transfer (CT) states may also be involved.<sup>30, 43</sup> The energy position of the  $T_1$  level determined from the phosphorescence spectrum of **Gd-1** was found at 22 620  $\text{cm}^{-1}$ , a value similar to the ones observed for the previously reported series of MCs possessing  $\text{Ga}^{3+}/\text{shi}$  scaffold, i.e.  $[\text{LnGa}_4(\text{shi})_4(\text{H}_2\text{shi})_2]$  (21 660  $\text{cm}^{-1}$ ),<sup>6</sup>  $[\text{LnGa}_4(\text{shi})_4(\text{benzoate})_4]$  (22 170  $\text{cm}^{-1}$ )<sup>5</sup> or  $[\text{Ln}_2\text{Ga}_8(\text{shi})_8(\text{isophthalate})_4]$  (21 190  $\text{cm}^{-1}$ ).<sup>3</sup> The  $T_1$  level in **Ln-1** is located slightly higher in energy than the emitting level of  $\text{Dy}^{3+}$ ,  $\Delta E(T_1 \leftarrow {}^4\text{F}_{9/2}) = 1\,520\, \text{cm}^{-1}$ , and a bit further from that of  $\text{Tb}^{3+}$ ,  $\Delta E(T_1 \leftarrow {}^5\text{D}_4) = 2\,220\, \text{cm}^{-1}$  (Figure 2). Relatively small difference in energy between the two levels increase the probability of thermally activated back  $T_1 \leftarrow \text{Ln}^{3+*}$  energy transfer. A clear influence of this process was confirmed for **Dy-1** with the 3.5 times lengthening of the average  $\tau_{\text{obs}}$  value upon cooling from room temperature to 10 K. In the case of **Tb-1**, this effect is insignificant and averaged  $\tau_{\text{obs}}$  values are similar at both temperatures. Back energy transfer is probably responsible for the bi-exponential character of luminescence decays observed for **Tb-1** and **Dy-1** (Table 1). For **Tm-1** in the solid state, emission is originating from different electronic levels (Figures 2, 3), i.e.  ${}^1\text{D}_2$  (28 000  $\text{cm}^{-1}$ ),  ${}^1\text{G}_4$  (21 350  $\text{cm}^{-1}$ ),  ${}^3\text{H}_4$  (12 700  $\text{cm}^{-1}$ ), and  ${}^3\text{H}_5$  (8 400  $\text{cm}^{-1}$ ). The  $T_1$  level is positioned well above the  ${}^3\text{H}_{4,5}$  levels but close to  ${}^1\text{G}_4$  ( $\Delta E(T_1 \leftarrow {}^1\text{G}_4) = 1\,270\, \text{cm}^{-1}$ ) and is significantly lower in energy than the  ${}^1\text{D}_2$  level ( $\Delta E(T_1 \leftarrow {}^1\text{D}_2) = -5\,380\, \text{cm}^{-1}$ ). The latter point suggests that  $\text{Tm}^{3+}$ -centered luminescence in **Tm-1** could be partially sensitized through the lowest singlet state of the ligands located at 28 690  $\text{cm}^{-1}$ . For **Pr-1**, most of the emission bands originate from the  ${}^1\text{D}_2$  (16 840  $\text{cm}^{-1}$ ) excited level, however transitions from the  ${}^3\text{P}_0$  (20 750  $\text{cm}^{-1}$ ) in the visible and the NIR ranges and from the  ${}^3\text{F}_3$  (6 500  $\text{cm}^{-1}$ ) in the NIR could also be detected (Figures 2, 3). Emitting levels of other studied  $\text{Ln}^{3+}$  are located at least 3 470  $\text{cm}^{-1}$  below the energy of the  $T_1$  level making it potentially well-adapted for their sensitization (Figure 2).

In the case of **Eu-1** in the solid state, the slight broadening to the red of the diffuse reflectance spectrum is an indication of the presence of a LMCT. Such electronic states, depending on their energy position, can either quench or enhance  $\text{Eu}^{3+}$  luminescence.<sup>45, 49, 98</sup> Contrary to all of the  $\text{Ga}^{3+}/\text{shi}$  systems previously described by us where the formation of LMCT states either significantly<sup>5</sup> or fully<sup>3, 6, 70</sup> quench  $\text{Eu}^{3+}$  emission, **Eu-1** exhibited pronounced red emission (Figure 3). Therefore, this series of  $[\text{LnGa}_8(\text{shi})_8(\text{OH})_4]$  MCs is the first  $\text{Ga}^{3+}/\text{shi}$  MC scaffold that can efficiently sensitize  $\text{Eu}^{3+}$  luminescence. This luminescence originating mainly from  ${}^5\text{D}_0 \rightarrow {}^7\text{F}_j$  ( $j = 0-6$ ) transitions is not only interesting for numerous practical applications<sup>52</sup> but also from a theoretical point of view.<sup>88</sup> The non-degenerate character of the emitting  ${}^5\text{D}_0$  level allows the easier interpretation of  $\text{Eu}^{3+}$  luminescence spectra. Therefore, the analysis of the relative intensities of  ${}^5\text{D}_0 \rightarrow {}^7\text{F}_j$  ( $j = 0-6$ ) transitions and their crystal-field splitting provide information about the point group symmetry and the coordination polyhedron around  $\text{Eu}^{3+}$ . Thus, interestingly, the emission spectrum of **Eu-1** in the solid state is domi-

nated by the  ${}^5\text{D}_0 \rightarrow {}^7\text{F}_4$  transition while the hypersensitive  ${}^5\text{D}_0 \rightarrow {}^7\text{F}_2$  and magnetic dipole  ${}^5\text{D}_0 \rightarrow {}^7\text{F}_1$  transitions have almost equal contributions (Figure 4, Table S4). These features reflect the square anti-prismatic environment around the  $\text{Eu}^{3+}$  and the presence of a pseudo- $D_{4h}$  symmetry,<sup>88</sup> in agreement with structural data. Further confirmation about the symmetry was obtained through the analysis of the fine splitting of the  ${}^5\text{D}_0 \rightarrow {}^7\text{F}_1$  transition into two-fold degenerate and non-degenerate components in the high-resolution spectrum (Figure S17). Moreover, the presence of a single narrow  ${}^5\text{D}_0 \rightarrow {}^7\text{F}_0$  transition (FWHM = 10  $\text{cm}^{-1}$ ) in the latter reflects the presence of only one type of emitting  $\text{Eu}^{3+}$  and therefore a unique and well-defined coordination environment around  $\text{Eu}^{3+}$  in **Eu-1**.

Dual emission of **Er-1** deserves a special attention. Multiple emitting levels and small energy gaps facilitating non-radiative deactivation processes make the design of luminescent  $\text{Er}^{3+}$  compounds with organic ligands highly challenging.<sup>30</sup> Nevertheless, potential applications in telecommunications<sup>34, 99</sup> of the  $\text{Er}^{3+} {}^4\text{I}_{13/2} \rightarrow {}^4\text{I}_{15/2}$  transition with an emission wavelength at  $\sim 1500\, \text{nm}$  have initiated multiple attempts to create and enhance  $\text{Er}^{3+}$  emission in coordination compounds.<sup>100-102</sup> The observation of  $\text{Er}^{3+}$  transitions in the visible range is uncommon and only a few examples could be found in the literature.<sup>56, 58, 103-104</sup> Nevertheless, we could unambiguously detect  ${}^2\text{H}_{11/2} \rightarrow {}^4\text{I}_{15/2}$  and  ${}^4\text{S}_{3/2} \rightarrow {}^4\text{I}_{15/2}$  transitions between 520 and 565 nm and as multiple bands in the range of 1450-1650 nm due to the  ${}^4\text{I}_{13/2} \rightarrow {}^4\text{I}_{15/2}$  transition in the emission spectrum of **Er-1** in the solid state (Figure 2).

In  $\text{CH}_3\text{OH}$  and  $\text{CD}_3\text{OD}$  solutions of **Ln-1** ( $\text{Ln} = \text{Nd}^{3+}, \text{Sm}^{3+}, \text{Eu}^{3+}, \text{Tb}^{3+}, \text{Dy}^{3+}, \text{Yb}^{3+}$ ) exhibit characteristic f-f transitions in the visible and/or NIR ranges upon excitation on chromophoric ligands at 310 nm. Compared to the corresponding emission spectra recorded in the solid state, a general trend was detected for all studied **Ln-1** in solution: the crystal-field splitting of f-f transitions remains the same while their relative intensities vary. The most significant change was observed for the **Eu-1** emission spectrum, which in the solid state is dominated by the  ${}^5\text{D}_0 \rightarrow {}^7\text{F}_4$  transition. However, in solution, this band has an equal intensity to the hypersensitive  ${}^5\text{D}_0 \rightarrow {}^7\text{F}_2$  transition (Figure 4, Table S4). Such variations are usually caused by changes in coordination environment and symmetry around  $\text{Ln}^{3+}$ .<sup>88</sup> However, NMR studies and ESI mass-spectrometry (*vide supra*) showed that the MC structure remains intact in solution while four  $\text{OH}^-$  bridges can be exchanged with  $\text{CH}_3\text{O}^-/\text{CD}_3\text{O}^-$ . Additionally, ESI mass spectrometry data show that, in solution, the solvation of the complex ion is likely to remove the coordination of two (1/2 equivalence)  $\text{Na}^+$  ions bound at one side of the complex. This situation may lead to a more symmetrical structure in solution than in the solid state. Such behavior can affect the global electronic structure of the MC scaffold and may explain the changes of relative intensities of f-f transitions. Phenomenological equations<sup>105</sup> were used to estimate the number of solvent molecules coordinated to the  $\text{Ln}^{3+}$  based on the difference in  $\tau_{\text{obs}}$  values recorded in both  $\text{CH}_3\text{OH}$  and  $\text{CD}_3\text{OD}$  solutions for **Eu-1**, **Tb-1**, and **Yb-1**. Results con-

firmed that this MC scaffold protects the coordinated  $\text{Ln}^{3+}$  ion well and no solvent molecules are directly coordinated. It should be noted, however, that in the case of **Nd-1**, luminescence decays become bi-exponential in solution possibly because of the partial coordination of solvent molecules. Such observation could be explained by  $\text{Nd}^{3+}$  having a larger ionic radius, providing additional space for the access of quenching solvent molecules.

Quantitative photophysical parameters, in particular the values of  $\tau_{\text{obs}}$  and  $Q_{\text{Ln}}^{\text{L}}$  for **Ln-1** in the solid state, are comparable or superior (for **Eu-1** and **Sm-1**) to those reported previously for the  $[\text{LnGa}_4(\text{shi})_4(\text{benzoate})_4]^5$  or  $[\text{Ln}_2\text{Ga}_8(\text{shi})_8(\text{isophthalate})_4]^3$  MCs (Table S7). In protic solvents, the values of  $\tau_{\text{obs}}$  and  $Q_{\text{Ln}}^{\text{L}}$  are usually lower than those measured in the solid state because of the higher probability of non-radiative deactivation through overtones of O–H vibrations.<sup>30</sup> Indeed, the values of  $Q_{\text{Ln}}^{\text{L}}$  measured for **Nd-1**, **Yb-1** and the NIR ( $^4\text{G}_{5/2} \rightarrow ^6\text{F}_J$ ) transitions of **Sm-1** are smaller in  $\text{CH}_3\text{OH}$  than in the solid state (Table 1). Nevertheless, the changes caused by the dissolution in a protic solvent are less significant than those reported previously for  $[\text{LnGa}_4(\text{shi})_4(\text{benzoate})_4]^5$ . Moreover, in the case of **Eu-1**, **Tb-1**, **Dy-1** or visible ( $^4\text{G}_{5/2} \rightarrow ^3\text{H}_J$ ) transitions of **Sm-1** the values of  $Q_{\text{Ln}}^{\text{L}}$  are, respectively, 3.7-, 1.4-, 5.5-times higher or the same in  $\text{CH}_3\text{OH}$  solution than in the solid state. It should be noted that  $Q_{\text{Sm}}^{\text{L}}$  of **Sm-1** in  $\text{CH}_3\text{OH}$  solution ( $\sim 10\%$ ) is exceptionally high since this value usually does not exceed 2% for  $\text{Sm}^{3+}$  complexes in protic solvents,<sup>106</sup> while  $Q_{\text{Yb}}^{\text{L}}$  of **Yb-1** is 3-times larger in respect to the value recorded for  $[\text{YbGa}_4(\text{shi})_4(\text{benzoate})_4]^5$  (Table 3). In deuterated  $\text{CD}_3\text{OD}$  solutions of **Ln-1**, the values of  $\tau_{\text{obs}}$  and  $Q_{\text{Ln}}^{\text{L}}$  are enhanced compared to those obtained in  $\text{CH}_3\text{OH}$  being in line with lower contribution of O–D vibrations to the non-radiative deactivation of  $\text{Ln}^{3+}$ .<sup>105</sup> This effect is the most sizable for **Sm-1** and **Yb-1**, the  $\tau_{\text{obs}}$  and  $Q_{\text{Ln}}^{\text{L}}$  of which increase by 8–12 times reaching values of 721  $\mu\text{s}/83\%$  and 196  $\mu\text{s}/8.4\%$ , respectively (Table 1). These values are exceptional for  $\text{Sm}^{3+}$  coordination compounds<sup>59, 106–108</sup> and are among the highest reported today for  $\text{Yb}^{3+}$  complexes formed with non-deuterated and non-halogenated ligands.<sup>51, 69, 109–111</sup>

To quantify the parameters that impact the total quantum yield ( $Q_{\text{Ln}}^{\text{L}}$ ) and to get a potential explanation for the photophysical properties of the studied series of  $\text{Ln}^{3+}/\text{Ga}^{3+}$  MCs, the values of  $\tau_{\text{rad}}$  were determined for **Eu-1** (Table 2) and **Yb-1** (Table 3) using Eqs. (3) and (4a,b), respectively. Further, knowing  $\tau_{\text{rad}}$ ,  $\tau_{\text{obs}}$  and  $Q_{\text{Ln}}^{\text{L}}$  (Table 1), it is possible to estimate intrinsic quantum yields ( $Q_{\text{Ln}}^{\text{L}}$ ) and sensitization efficiencies of the ligands,  $\eta_{\text{sens}}$ , according to Eq. (1).

It was found that  $\tau_{\text{rad}}$  is equal to 2.78 ms for **Eu-1** in the solid state, a value that is close to the one reported, for example, for  $\text{Eu}^{3+}$  complexes formed with benzothiazole-substituted pyridine-2-carboxylate ligands (2.7–3.2 ms).<sup>112</sup> In  $\text{CH}_3\text{OH}$  or  $\text{CD}_3\text{OD}$  solutions, the value of  $\tau_{\text{rad}}$  becomes 2.8-times longer (7.8 ms). Similar values were reported for aqueous solutions of  $\text{Eu}^{3+}$  helicates with pseudo- $D_3$  symmetry (6.2–6.9 ms).<sup>113</sup> Such changes of  $\tau_{\text{rad}}$  are most probably induced by an exchange of four  $\text{OH}^-$  bridges with  $\text{CH}_3\text{O}^-/\text{CD}_3\text{O}^-$  in solution as suggested by mass-

spectrometry data (*vide supra*). The lengthening of  $\tau_{\text{rad}}$  leads to a decrease of  $Q_{\text{Eu}}^{\text{L}}$  by 1.5–2 times in solution compared to the value obtained in the solid state. Nevertheless, significantly improved  $\eta_{\text{sens}}$  (7.3–7.6 fold) in solutions of **Eu-1** results in a 3.7–5 times enhancement of  $Q_{\text{Eu}}^{\text{L}}$ .

In the case of **Yb-1**, the different photophysical parameters obtained in  $\text{CH}_3\text{OH}$  or  $\text{CD}_3\text{OD}$  solutions could be compared with the values reported for  $[\text{YbGa}_4(\text{shi})_4(\text{benzoate})_4]^5$  and  $[\text{YbGa}_4(\text{shi})_4(\text{H}_2\text{shi})_2]^6$  (Table 3). The values of  $\tau_{\text{rad}}$  for **Yb-1** are 1.4–1.5 times longer than for the other  $\text{Yb}^{3+}/\text{Ga}^{3+}$  MCs, probably, due to the higher level of symmetry around  $\text{Yb}^{3+}$  for the former one (pseudo- $D_{4h}$  vs. pseudo- $C_4$  or  $C_1$ ). However, the values of  $Q_{\text{Yb}}^{\text{L}}$  are significantly (4.9–6.6 fold) higher for **Yb-1** than for the  $[\text{YbGa}_4(\text{shi})_4(\text{benzoate})_4]$  and  $[\text{YbGa}_4(\text{shi})_4(\text{H}_2\text{shi})_2]$  MCs because of the longer  $\tau_{\text{obs}}$ . Notably, these two parameters observed for **Yb-1** are similar to the ones reported for  $\text{Yb}^{3+}/\text{Zn}^{2+}$  “encapsulated sandwich” MCs with quinaldichydroxamic acid, which similarly have a  $D_{4h}$  type symmetry.<sup>114</sup> Finally, sensitization efficiencies for **Yb-1** are comparable or slightly lower than in  $[\text{YbGa}_4(\text{shi})_4(\text{benzoate})_4]$  and  $[\text{YbGa}_4(\text{shi})_4(\text{H}_2\text{shi})_2]$ . Together with improved  $Q_{\text{Yb}}^{\text{L}}$  and  $\tau_{\text{obs}}$  for **Yb-1**, we observed a more than 3.5–6.5 times enhancement of  $Q_{\text{Yb}}^{\text{L}}$  values in solution relative to the aforementioned  $\text{Ln}^{3+}/\text{Ga}^{3+}$  complexes.

Apart from the energy positions of the feeding levels ( $T_1$ ,  $S_1$ , CT) with respect to accepting  $\text{Ln}^{3+}$  levels, another aspect that is usually considered when designing luminescent  $\text{Ln}^{3+}$ -based coordination compounds is to avoid the presence of O–H, N–H or C–H oscillator in close proximity to  $\text{Ln}^{3+}$  to prevent the quenching of their excited states. Therefore, the closest distances from  $\text{Ln}^{3+}$  to these oscillators were estimated for **Ln-1** (Figure S2). It was found that  $\text{Ln}\cdots\text{C–H}$  is  $\sim 7$  Å, a value that is close to the one determined for  $\text{Ln}^{3+}/\text{Zn}^{2+}$  “encapsulated sandwich” MCs<sup>114</sup> and longer than that in  $[\text{LnGa}_4(\text{shi})_4(\text{benzoate})_4]^5$  or  $[\text{Ln}_2\text{Ga}_8(\text{shi})_8(\text{isophthalate})_4]^3$  (3.4–3.6 Å). However, the presence of O–H groups at  $\sim 4$  Å to  $\text{Ln}^{3+}$  in the crystal structure of **Ln-1** represents a source of non-radiative deactivations and is probably the reason for the slightly lower  $Q_{\text{Ln}}^{\text{L}}$  values for some of the **Ln-1** in the solid state compared to the  $[\text{LnGa}_4(\text{shi})_4(\text{benzoate})_4]^5$  or  $[\text{Ln}_2\text{Ga}_8(\text{shi})_8(\text{isophthalate})_4]^3$  MCs. On the other hand, in methanol solutions of **Ln-1**, while the molecular structure is preserved, four  $\text{OH}^-$  bridges are exchanged with  $\text{CH}_3\text{O}^-/\text{CD}_3\text{O}^-$  minimizing the sources of non-radiative deactivations that may explain comparable or higher  $Q_{\text{Ln}}^{\text{L}}$  in respect to those of the aforementioned  $\text{Ln}^{3+}/\text{Ga}^{3+}$ .

## CONCLUSIONS

We have created, synthesized and characterized a new series of  $(\text{Ga}^{3+})_2\text{Ln}^{3+}$  MCs (**Ln-1** where  $\text{Ln} = \text{Y}^{3+}, \text{Pr}^{3+}, \text{Nd}^{3+}, \text{Sm}^{3+}, \text{Eu}^{3+}, \text{Gd}^{3+}, \text{Tb}^{3+}, \text{Dy}^{3+}, \text{Ho}^{3+}, \text{Er}^{3+}, \text{Tm}^{3+}$  and  $\text{Er}^{3+}$ ) with the general composition  $[\text{LnGa}_8(\text{shi})_8(\text{OH})_4]\text{Na}_x\text{CH}_3\text{OH}\cdot y\text{H}_2\text{O}$  that possesses a pseudo- $D_{4h}$  symmetry about the central  $\text{Ln}^{3+}$ . **Ln-1** in the solid state possess unique photophysical properties. In particular, this is the first example among different series of

Ga<sup>3+</sup>/Ln<sup>3+</sup> MCs reported so far that exhibits an intense red Eu<sup>3+</sup>-centered emission. Moreover, **Ln-1** contain the first MCs that demonstrate the exceptional ability to sensitize the emissions of six Ln<sup>3+</sup> in a dual range of wavelengths (visible and NIR: Pr<sup>3+</sup>, Sm<sup>3+</sup>, Dy<sup>3+</sup>, Ho<sup>3+</sup>, Er<sup>3+</sup> and Tm<sup>3+</sup>). In addition, **Yb-1** and **Nd-1** show characteristic emission in the NIR range while **Tb-1** exhibits bright green luminescence. Therefore, **Ln-1** is one of the few single-molecular complexes able to sensitize f-f transitions of ten out of fifteen trivalent lanthanide(III) ions, excluding La<sup>3+</sup> (4f<sup>0</sup>), Ce<sup>3+</sup> (impeding 4f-5d transitions), Pm<sup>3+</sup> (radioactive), Gd<sup>3+</sup> (UV emission), and Lu<sup>3+</sup> (4f<sup>14</sup>). In addition, the structure of **Ln-1** remains intact in methanol solutions while four OH<sup>-</sup> bridges are exchanged with CH<sub>3</sub>O<sup>-</sup>/CD<sub>3</sub>O<sup>-</sup> leading to comparable or improved photophysical properties as demonstrated for Ln = Nd<sup>3+</sup>, Sm<sup>3+</sup>, Eu<sup>3+</sup>, Tb<sup>3+</sup>, Dy<sup>3+</sup>, and Yb<sup>3+</sup>. The values of  $Q_{Ln}^L$  for **Sm-1** in the visible range are exceptionally high when recorded in both protic (CH<sub>3</sub>OH, 10%) and deuterated solvents (CD<sub>3</sub>OD, 83%) while those of **Yb-1** are among the highest reported today for Yb<sup>3+</sup> complexes with non-deuterated and non-halogenated ligands. These results demonstrate that LnGa<sub>8</sub>(shi)<sub>8</sub>(OH)<sub>4</sub> MCs are able to protect and sensitize Ln<sup>3+</sup> emission throughout the visible and the NIR ranges opening new and broad perspectives for the exciting applications requiring such exceptional properties. This molecular system offers for the first time a large choice of lanthanide(III) emitters operating simultaneously in dual visible and NIR ranges, providing even more unique spectroscopic signatures.

## ASSOCIATED CONTENT

**Supporting Information.** The Supporting Information is available free of charge at <http://pubs.acs.org>. Experimental details, synthesis and characterization of **Ln-1** MCs, X-ray crystallographic parameters, including CIF file (CCDC 2008321), ESI mass-spectra, NMR studies, supplementary tables and figures describing photophysical properties.

## AUTHOR INFORMATION

### \*Corresponding Authors

Vincent L. Pecoraro - *Department of Chemistry, Willard H. Dow Laboratories, University of Michigan, Ann Arbor, Michigan 48109, USA*; Email: [vlpec@umich.edu](mailto:vlpec@umich.edu)

Stéphane Petoud - *Centre de Biophysique Moléculaire, CNRS UPR 4301, F-45071 Orleans Cedex 2, France*. Email: [stephane.petoud@inserm.fr](mailto:stephane.petoud@inserm.fr)

Svetlana V. Eliseeva - *Centre de Biophysique Moléculaire, CNRS UPR 4301, F-45071 Orleans Cedex 2, France*. Email: [svetlana.eliseeva@cnrs-orleans.fr](mailto:svetlana.eliseeva@cnrs-orleans.fr)

### Authors

Elvin V. Salerno - *Department of Chemistry, Willard H. Dow Laboratories, University of Michigan, Ann Arbor, Michigan 48109, USA*.

Bernadette L. Schneider - *Department of Chemistry, Willard H. Dow Laboratories, University of Michigan, Ann Arbor, Michigan 48109, USA*.

Jeff W. Kampf - *Department of Chemistry, Willard H. Dow Laboratories, University of Michigan, Ann Arbor, Michigan 48109, USA*.

## Author Contributions

‡These authors contributed equally.

## ACKNOWLEDGMENTS

This research was supported in part by the National Science Foundation (NSF) under the grant CHE-1664964 (V.L.P.). Acknowledgement is made for funding from NSF grant CHE-0840456 for X-ray instrumentation. E.V.S. thanks the Rackham Graduate School for international travel funding as well as NSF grant DGE-1256260. The work in France was supported by La Ligue Contre le Cancer and La Région Centre. S.P. acknowledges support from the Institut National de la Santé et de la Recherche Médicale (INSERM).

## REFERENCES

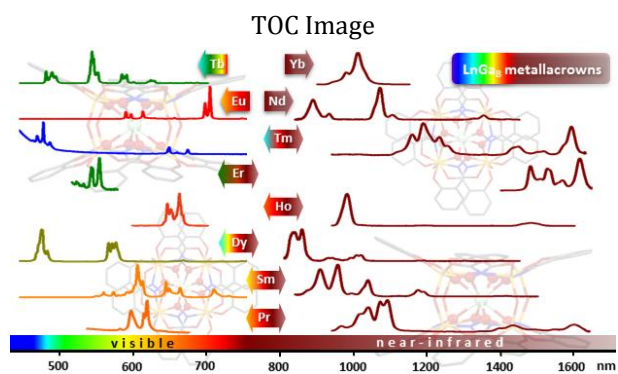
- Lutter, J. C.; Zaleski, C. M.; Pecoraro, V. L., *Metallacrowns: Supramolecular Constructs With Potential in Extended Solids, Solution-State Dynamics, Molecular Magnetism, and Imaging*. In *Advances in Inorganic Chemistry*, 2018; Vol. 71, pp 177-246.
- Mezei, G.; Zaleski, C. M.; Pecoraro, V. L., Structural and functional evolution of metallacrowns. *Chem. Rev.* **2007**, *107* (11), 4933-5003.
- Nguyen, T. N.; Chow, C. Y.; Eliseeva, S. V.; Trivedi, E. R.; Kampf, J. W.; Martinić, I.; Petoud, S.; Pecoraro, V. L., One-Step Assembly of Visible and Near-Infrared Emitting Metallacrown Dimers Using a Bifunctional Linker. *Chem. Eur. J.* **2018**, *5*, 1031-1035.
- Lah, M. S.; Gibney, B. R.; Tierney, D. L.; Penner-Hahn, J. E.; Pecoraro, V. L., The fused metallacrown anion Na<sub>2</sub>{[Na<sub>0.5</sub>[Ga(salicylhydroximate)]<sub>4</sub>]<sub>2</sub>(μ<sub>2</sub>-OH)<sub>4</sub>}<sup>-</sup> is an inorganic analog of a cryptate. *J. Am. Chem. Soc.* **1993**, *115* (13), 5857-5858.
- Chow, C. Y.; Eliseeva, S. V.; Trivedi, E. R.; Nguyen, T. N.; Kampf, J. W.; Petoud, S.; Pecoraro, V. L., Ga<sup>3+</sup>/Ln<sup>3+</sup> Metallacrowns: A Promising Family of Highly Luminescent Lanthanide Complexes That Covers Visible and Near-Infrared Domains. *J. Am. Chem. Soc.* **2016**, *138* (15), 5100-5109.
- Nguyen, T. N.; Eliseeva, S. V.; Chow, C. Y.; Kampf, J. W.; Petoud, S.; Pecoraro, V. L., Peculiarities of crystal structures and photophysical properties of Ga<sup>III</sup>/Ln<sup>III</sup> metallacrowns with a non-planar [12-MC-4] core. *Inorg. Chem. Front.* **2020**, *7*, 1553-1563.
- Teo, P.; Koh, L. L.; Hor, T. S., Na<sup>+</sup> and Ca<sup>2+</sup> ion selective pyridylcarboxylate rings of Pd(II) and Pt(II). *Dalton Trans.* **2009**, (29), 5637-5646.
- Cutland, A. D.; Malkani, R. G.; Kampf, J. W.; Pecoraro, V. L., Lanthanide 15-metallacrown-5 complexes form nitrate-selective chiral cavities. *Angew. Chem. Int. Ed.* **2000**, *39* (15), 2689-2691.
- Lim, C.-S.; Jankolovits, J.; Zhao, P.; Kampf, J. W.; Pecoraro, V. L., Gd(III) 15-metallacrown-5 recognition of chiral alpha-amino acid analogues. *Inorg. Chem.* **2011**, *50* (11), 4832-4841.
- Grant, J. T.; Jankolovits, J.; Pecoraro, V. L., Enhanced guest affinity and enantioselectivity through variation of the Gd<sup>3+</sup> 15-metallacrown-5 side chain. *Inorg. Chem.* **2012**, *51* (15), 8034-8041.

11. Sgarlata, C.; Giuffrida, A.; Trivedi, E. R.; Pecoraro, V. L.; Arena, G., Anion encapsulation drives the formation of dimeric Gd(III)[15-metallacrown-5](3+) complexes in aqueous solution. *Inorg. Chem.* **2017**, *56* (9), 4771-4774.
12. Jankolovits, J.; Lim, C. S.; Mezei, G.; Kampf, J. W.; Pecoraro, V. L., Influencing the size and anion selectivity of dimeric Ln<sup>3+</sup> 15-metallacrown-5 compartments through systematic variation of the host side chains and central metal. *Inorg. Chem.* **2012**, *51* (8), 4527-4538.
13. Jankolovits, J.; Van-Noord, A. D. C.; Kampf, J. W.; Pecoraro, V. L., Selective anion encapsulation in solid-state Ln(III)[15-metallacrown-5]<sup>3+</sup> compartments through secondary sphere interactions. *Dalton Trans.* **2013**, *42* (27), 9803-9808.
14. Piotrowski, H.; Polborn, K.; Hilt, G.; Severin, K., A self-assembled metallomacrocyclic ionophore with high affinity and selectivity for Li<sup>+</sup> and Na<sup>+</sup>. *J. Am. Chem. Soc.* **2001**, *123* (11), 2699-2700.
15. Chow, C. Y.; Bolvin, H.; Campbell, V. E.; Guillot, R.; Kampf, J. W.; Wernsdorfer, W.; Gendron, F.; Autschbach, J.; Pecoraro, V. L.; Mallah, T., Assessing the exchange coupling in binuclear lanthanide(III) complexes and the slow relaxation of the magnetization in the antiferromagnetically coupled Dy<sub>2</sub> derivative. *Chem. Sci.* **2015**, *6* (7), 4148-4159.
16. Boron, T. T.; Lutter, J. C.; Daly, C. I.; Chow, C. Y.; Davis, A. H.; Nimthong-Roldán, A.; Zeller, M.; Kampf, J. W.; Zaleski, C. M.; Pecoraro, V. L., The Nature of the Bridging Anion Controls the Single-Molecule Magnetic Properties of DyX<sub>4</sub>M 12-Metallacrown-4 Complexes. *Inorg. Chem.* **2016**, *55* (20), 10597-10607.
17. Zaleski, C. M.; Tricard, S.; Depperman, E. C.; Wernsdorfer, W.; Mallah, T.; Kirk, M. L.; Pecoraro, V. L., Single molecule magnet behavior of a pentanuclear mn-based metallacrown complex: solid state and solution magnetic studies. *Inorg. Chem.* **2011**, *50* (22), 11348-11352.
18. Zaleski, C. M.; Depperman, E. C.; Kampf, J. W.; Kirk, M. L.; Pecoraro, V. L., Using Ln(III)[15-MC<sub>Cu(II)(N)(S)-pheHA-5</sub>]<sup>3+</sup> complexes to construct chiral single-molecule magnets and chains of single-molecule magnets. *Inorg. Chem.* **2006**, *45* (25), 10022-10024.
19. Zaleski, C. M.; Depperman, E. C.; Dendrinou-Samara, C.; Alexiou, M.; Kampf, J. W.; Kessissoglou, D. P.; Kirk, M. L.; Pecoraro, V. L., Metallacryptate Single-Molecule Magnets: Effect of Lower Molecular Symmetry on Blocking Temperature. *J. Am. Chem. Soc.* **2005**, *127* (37), 12862-12872.
20. Zaleski, C. M.; Depperman, E. C.; Kampf, J. W.; Kirk, M. L.; Pecoraro, V. L., Synthesis, Structure, and Magnetic Properties of a Large Lanthanide-Transition-Metal Single-Molecule Magnet. *Angew. Chem. Int. Ed.* **2004**, *43* (30), 3912-3914.
21. Boron, T. T.; Kampf, J. W.; Pecoraro, V. L., A Mixed 3d-4f 14-Metallacrown-5 Complex That Displays Slow Magnetic Relaxation through Geometric Control of Magnetoanisotropy. *Inorg. Chem.* **2010**, *49* (20), 9104-9106.
22. Happ, P.; Rentschler, E., Enforcement of a high-spin ground state for the first 3d heterometallic 12-metallacrown-4 complex. *Dalton Trans.* **2014**, *43* (41), 15308-15312.
23. Happ, P.; Plenk, C.; Rentschler, E., 12-MC-4 metallacrowns as versatile tools for SMM research. *Coord. Chem. Rev.* **2015**, *289-290*, 238-260.
24. Chow, C. Y.; Guillot, R.; Rivière, E.; Kampf, J. W.; Mallah, T.; Pecoraro, V. L., Synthesis and Magnetic Characterization of Fe(III)-Based 9-Metallacrown-3 Complexes Which Exhibit Magnetorefrigerant Properties. *Inorg. Chem.* **2016**, *55* (20), 10238-10247.
25. Muravyeva, M. S.; Zabrodina, G. S.; Samsonov, M. A.; Kluev, E. A.; Khrapichev, A. A.; Katkova, M. A.; Mukhina, I. V., Water-soluble tetraaqua Ln(III) glycinehydroximate 15-metallacrown-5 complexes towards potential MRI contrast agents for ultra-high magnetic field. *Polyhedron* **2016**, *114*, 165-171.
26. Katkova, M. A.; Zabrodina, G. S.; Muravyeva, M. S.; Shavyrin, A. S.; Baranov, E. V.; Khrapichev, A. A.; Ketkov, S. Y., Facile one-pot route toward water-soluble lanthanide-copper-glycinehydroximate 15-metallacrown-5 complexes. *Eur. J. Inorg. Chem.* **2015**, (31), 5202-5208.
27. Parac-Vogt, T. N.; Pacco, A.; Nockemann, P.; Laurent, S.; Muller, R. N.; Wickleder, M.; Meyer, G.; Vander Elst, L.; Binnemans, K., Relaxometric study of copper [15]metallacrown-5 gadolinium complexes derived from alpha-aminohydroxamic acids. *Chem. Eur. J.* **2006**, *12* (1), 204-10.
28. Martinić, I.; Eliseeva, S. V.; Nguyen, T. N.; Foucher, F.; Gosset, D.; Westall, F.; Pecoraro, V. L.; Petoud, S., Near-Infrared Luminescent Metallacrowns for Combined in vitro Cell Fixation and Counter Staining. *Chemical Science* **2017**, *8* (9), 6042-6050.
29. Martinić, I.; Eliseeva, S. V.; Nguyen, T. N.; Pecoraro, V. L.; Petoud, S., Near-Infrared Optical Imaging of Necrotic Cells by Photostable Lanthanide-Based Metallacrowns. *J. Am. Chem. Soc.* **2017**, *139* (25), 8388-8391.
30. Bünzli, J.-C. G.; Eliseeva, S. V., Photophysics of Lanthanoid Coordination Compounds. In *Comprehensive Inorganic Chemistry II*, Yam, V. W.-W., Ed. Elsevier B.V.: Amsterdam, 2013; Vol. 8, pp 339-398.
31. Binnemans, K., Lanthanide-Based Luminescent Hybrid Materials. *Chem. Rev.* **2009**, *109* (9), 4283-4374.
32. Bünzli, J.-C. G., Lanthanide Luminescence for Biomedical Analyses and Imaging. *Chem. Rev.* **2010**, *110* (5), 2729-2755.
33. Eliseeva, S. V.; Bünzli, J.-C. G., Lanthanide luminescence for functional materials and bio-sciences. *Chem. Soc. Rev.* **2010**, *39* (1), 189-227.
34. Ye, H. Q.; Li, Z.; Peng, Y.; Wang, C. C.; Li, T. Y.; Zheng, Y. X.; Sapelkin, A.; Adamopoulos, G.; Hernandez, I.; Wyatt, P. B.; Gillin, W. P., Organo-erbium systems for optical amplification at telecommunications wavelengths. *Nature Mater.* **2014**, *13* (4), 382-386.
35. Guillou, O.; Daiguebonne, C.; Calvez, G.; Bernot, K., A Long Journey in Lanthanide Chemistry: From Fundamental Crystallogensis Studies to Commercial Anticounterfeiting Taggants. *Acc. Chem. Res.* **2016**, *49* (5), 844-56.
36. SeethaLekshmi, S.; Ramya, A. R.; Reddy, M. L. P.; Varughese, S., Lanthanide complex-derived white-light emitting solids: A survey on design strategies. *J. Photochem. Photobiol. C: Photochem. Rev.* **2017**, *33*, 109-131.
37. Wang, L.; Zhao, Z.; Wei, C.; Wei, H.; Liu, Z.; Bian, Z.; Huang, C., Review on the Electroluminescence Study of Lanthanide Complexes. *Adv. Opt. Mater.* **2019**, *7* (11), 1801256.
38. Ning, Y. Y.; Zhu, M. L.; Zhang, J. L., Near-infrared (NIR) lanthanide molecular probes for bioimaging and biosensing. *Coord. Chem. Rev.* **2019**, *399*, 213028.
39. Martinić, I.; Eliseeva, S. V.; Petoud, S., Near-infrared emitting probes for biological imaging: Organic fluorophores, quantum dots, fluorescent proteins, lanthanide(III) complexes and nanomaterials. *J. Lumin.* **2017**, *189*, 19-43.

40. Mathieu, E.; Sipos, A.; Demeyere, E.; Phipps, D.; Sakaveli, D.; Borbas, K. E., Lanthanide-based tools for the investigation of cellular environments. *Chem. Commun.* **2018**, 54 (72), 10021-10035.
41. Sy, M.; Nonat, A.; Hildebrandt, N.; Charbonniere, L. J., Lanthanide-based luminescence biolabelling. *Chem. Commun.* **2016**, 52, 5080-5095.
42. Weissman, S. I., Intramolecular Energy Transfer The Fluorescence of Complexes of Europium. *J. Chem. Phys.* **1942**, 10 (4), 214-217.
43. Carneiro Neto, A. N.; Teotonio, E. E. S.; de Sá, G. F.; Brito, H. F.; Legendziewicz, J.; Carlos, L. D.; Felinto, M. C. F. C.; Gawryszewska, P.; Moura, R. T.; Longo, R. L.; et.al., Modeling intramolecular energy transfer in lanthanide chelates: A critical review and recent advances. In *Handbook on the Physics and Chemistry of Rare Earths*, Bünzli, J.-C. G.; Pecharsky, V., Eds. 2019; Vol. 56, pp 55-162.
44. Junker, A. K. R.; Sørensen, T. J., Shining light on the excited state energy cascade in kinetically inert Ln(III) complexes of a coumarin-appended D03A ligand. *Dalton Trans.* **2019**, 48 (3), 964-970.
45. D'Aleo, A.; Pointillart, F.; Ouahab, L.; Andraud, C.; Maury, O., Charge transfer excited states sensitization of lanthanide emitting from the visible to the near-infra-red. *Coord. Chem. Rev.* **2012**, 256 (15-16), 1604-1620.
46. Lo, W. S.; Zhang, J.; Wong, W. T.; Law, G. L., Highly luminescent Sm(III) complexes with intraligand charge-transfer sensitization and the effect of solvent polarity on their luminescent properties. *Inorg. Chem.* **2015**, 54 (8), 3725-3727.
47. Pan, M.; Du, B. B.; Zhu, Y. X.; Yue, M. Q.; Wei, Z. W.; Su, C. Y., Highly Efficient Visible-to-NIR Luminescence of Lanthanide(III) Complexes with Zwitterionic Ligands Bearing Charge-Transfer Character: Beyond Triplet Sensitization. *Chem. Eur. J.* **2016**, 22 (7), 2440-51.
48. Zhang, Z.; Zhou, Y.; Li, H.; Gao, T.; Yan, P., Visible light sensitized near-infrared luminescence of ytterbium via ILCT states in quadruple-stranded helicates. *Dalton Trans.* **2019**, 48 (12), 4026-4034.
49. Nonat, A.; Esteban-Gomez, D.; Valencia, L.; Perez-Lourido, P.; Barriada, J. L.; Charbonniere, L. J.; Platas-Iglesias, C., The role of ligand to metal charge-transfer states on the luminescence of europium complexes with 18-membered macrocyclic ligands. *Dalton Trans.* **2019**, 48 (12), 4035-4045.
50. Liao, W.-M.; Li, C.-J.; Wu, X.; Zhang, J.-H.; Wang, Z.; Wang, H.-P.; Fan, Y.-N.; Pan, M.; Su, C.-Y., Homometallic Ln(III)-complexes from an ILCT ligand with sensitized vis-NIR emission, excitation-dependent PL color tuning and white-light emission. *J. Mater. Chem. C* **2018**, 6 (13), 3254-3259.
51. Bünzli, J.-C. G., On the design of highly luminescent lanthanide complexes. *Coord. Chem. Rev.* **2015**, 293-294, 19-47.
52. Shuvaev, S.; Starck, M.; Parker, D., Responsive, Water-Soluble Europium(III) Luminescent Probes. *Chem. Eur. J.* **2017**, 23 (42), 9974-9989.
53. Hildebrandt, N.; Wegner, K. D.; Algar, W. R., Luminescent terbium complexes: Superior Förster resonance energy transfer donors for flexible and sensitive multiplexed biosensing. *Coord. Chem. Rev.* **2014**, 273-274, 125-138.
54. Petoud, S.; Cohen, S. M.; Bünzli, J.-C. G.; Raymond, K. N., Stable, high quantum yield lanthanide luminescence agents: multidentate 2-hydroxyisophthalamide complexes of Sm(III), Eu(III), Tb(III), Dy(III) in aqueous solution. *J. Am. Chem. Soc.* **2003**, 125 (44), 13324-13325.
55. Liu, G. K., Electronic Energy Level Structure. In *Spectroscopic Properties of Rare Earths in Optical Materials*, Liu, G. K.; Jacquier, B., Eds. Springer Verlag: Berlin, 2005; Vol. 83, pp 1-94.
56. Sedykh, A. E.; Kurth, D. G.; Müller-Buschbaum, K., Two Series of Lanthanide Coordination Polymers and Complexes with 4'-Phenylterpyridine and their Luminescence Properties. *Eur. J. Inorg. Chem.* **2019**, 2019 (42), 4564-4571.
57. Biju, S.; Gopakumar, N.; Bünzli, J.-C. G.; Scopelliti, R.; Kim, H. K.; Reddy, M. L. P., Brilliant Photoluminescence and Triboluminescence from Ternary Complexes of Dy<sup>III</sup> and Tb<sup>III</sup> with 3-Phenyl-4-Propanoyl-5-Isoxazolone and a Bidentate Phosphine Oxide Coligand. *Inorg. Chem.* **2013**, 52 (15), 8750-8758.
58. Golesorkhi, B.; Guenee, L.; Nozary, H.; Fürstenberg, A.; Suffren, Y.; Eliseeva, S. V.; Petoud, S.; Hauser, A.; Piguet, C., Thermodynamic Programming of Erbium(III) Coordination Complexes for Dual Visible/Near-Infrared Luminescence. *Chem. Eur. J.* **2018**, 24 (50), 13158-13169.
59. Ahmed, Z.; Iftikhar, K., Red, orange-red and near-infrared light emitting ternary lanthanide tris  $\beta$ -diketonate complexes with distorted C<sub>4v</sub> geometrical structures. *Dalton Trans.* **2019**, 48 (15), 4973-4986.
60. Chen, L.; Zhang, H.; Pan, M.; Wei, Z. W.; Wang, H. P.; Fan, Y. N.; Su, C. Y., An Efficient Visible and Near-Infrared (NIR) Emitting Sm(III) Metal-Organic Framework (Sm-MOF) Sensitized by Excited-State Intramolecular Proton Transfer (ESIPT) Ligand. *Chem. Asian J.* **2016**, 11 (12), 1765-9.
61. Dang, S.; Yu, J.; Yu, J.; Wang, X.; Sun, L.; Feng, J.; Fan, W.; Zhang, H., Novel Holmium (Ho) and Praseodymium (Pr) ternary complexes with fluorinated-ligand and 4,5-diazafluoren-9-one. *Mater. Lett.* **2011**, 65 (11), 1642-1644.
62. Eliseeva, S. V.; Liasotkyi, V. S.; Golovach, I. P.; Doga, P. G.; Antonovich, V. P.; Petoud, S.; Meshkova, S. B., Exploring the ability of the nalidixate to sensitize visible and near-infrared emitting lanthanide(III) cations. *Methods Appl. Fluoresc.* **2017**, 5 (1), 014002.
63. Wang, J.; Suffren, Y.; Daiguebonne, C.; Freslon, S.; Bernot, K.; Calvez, G.; Le Pollès, L.; Roiland, C.; Guillou, O., Multi-Emissive Lanthanide-Based Coordination Polymers for Potential Application as Luminescent Bar-Codes. *Inorg. Chem.* **2019**, 58 (4), 2659-2668.
64. Du, B. B.; Zhu, Y. X.; Pan, M.; Yue, M. Q.; Hou, Y. J.; Wu, K.; Zhang, L. Y.; Chen, L.; Yin, S. Y.; Fan, Y. N.; Su, C. Y., Direct white-light and a dual-channel barcode module from Pr(III)-MOF crystals. *Chem. Commun.* **2015**, 51 (63), 12533-6.
65. Wang, S.; Xu, J.; Wang, J.; Wang, K.-Y.; Dang, S.; Song, S.; Liu, D.; Wang, C., Luminescence of samarium(III) bis-dithiocarbamate frameworks: codoped lanthanide emitters that cover visible and near-infrared domains. *J. Mater. Chem. C* **2017**, 5 (26), 6620-6628.
66. White, K. A.; Chengelis, D. A.; Gogick, K. A.; Stehman, J.; Rosi, N. L.; Petoud, S., Near-Infrared Luminescent Lanthanide MOF Barcodes. *J. Am. Chem. Soc.* **2009**, 131 (50), 18069-18071.
67. Foucault-Collet, A.; Shade, C. M.; Nazarenko, I.; Petoud, S.; Eliseeva, S. V., Polynuclear Sm(III) polyamidoamine-based dendrimer: a single probe for combined visible and near-infrared live-cell imaging. *Angew. Chem. Int. Ed.* **2014**, 53 (11), 2927-30.

68. Bui, A. T.; Grichine, A.; Brasselet, S.; Duperray, A.; Andraud, C.; Maury, O., Unexpected Efficiency of a Luminescent Samarium(III) Complex for Combined Visible and Near-Infrared Biphononic Microscopy. *Chem. Eur. J.* **2015**, *21* (49), 17757-61.
69. Lutter, J. C.; Eliseeva, S. V.; Collet, G.; Martinić, I.; Kampf, J. W.; Schneider, B. L.; Carichner, A.; Sobilo, J.; Lerondel, S.; Petoud, S.; Pecoraro, V. L., Iodinated metallacrowns: toward combined bimodal near-infrared and X-ray contrast imaging agents. *Chem. Eur. J.* **2020**, *26* (6), 1274-1277.
70. Lutter, J. C.; Eliseeva, S. V.; Kampf, J. W.; Petoud, S.; Pecoraro, V. L., A Unique Ln(III){[3.3.1]Ga(III) Metallacryptate} Series that Possesses Properties of Slow Magnetic Relaxation and Visible/Near-Infrared Luminescence. *Chem. Eur. J.* **2018**, *24*, 10773-10783.
71. Athanasopoulou, A. A.; Baldovi, J. J.; Carrella, L. M.; Rentschler, E., Field-induced slow magnetic relaxation in the first Dy(III)-centered 12-metallacrown-4 double-decker. *Dalton Trans.* **2019**, *48* (41), 15381-15385.
72. Gao, D., Acidities of Water and Methanol in Aqueous Solution and DMSO. *J. Chem. Ed.* **2009**, *86* (7), 864-868.
73. Cohen, Y.; Avram, L.; Frish, L., Diffusion NMR spectroscopy in supramolecular and combinatorial chemistry: an old parameter - new insights. *Angew. Chem. Int. Ed.* **2005**, *44* (4), 520-554.
74. Zuccaccia, D.; Macchioni, A., An Accurate Methodology to Identify the Level of Aggregation in Solution by PGSE NMR Measurements: The Case of Half-Sandwich Diamino Ruthenium(II) Salts. *Organometallics* **2005**, *24* (14), 3476-3486.
75. Cameron, K. S.; Fielding, L., NMR Diffusion Spectroscopy as a Measure of Host-Guest Complex Association Constants and as a Probe of Complex Size. *J. Org. Chem.* **2001**, *66* (21), 6891-6895.
76. Lutter, J. C. Refining Lanthanide Luminescence in Metallacrowns by Systematic Alteration of Hydroximate Ligand. University of Michigan, 2018.
77. Carnall, W. T.; Fields, P. R.; Rajnak, K., Electronic Energy Levels in the Trivalent Lanthanide Aquo Ions II. Gd(III). Absorption Spectra. *J. Chem. Phys.* **1968**, *49*, 4443-4446.
78. Tobita, S.; Arakawa, M.; Tanaka, I., The paramagnetic metal effect on the ligand localized S1-to-T1 intersystem crossing in rare earth metal complexes with methyl salicylate. *J. Phys. Chem.* **1985**, *89*, 5649-5654.
79. Carnall, W. T.; Fields, P. R.; Rajnak, K., Electronic Energy Levels in the Trivalent Lanthanide Aquo Ions IV. Eu(III). Absorption Spectra. *J. Chem. Phys.* **1968**, *49*, 4450-4455.
80. Carnall, W. T.; Fields, P. R.; Rajnak, K., Electronic Energy Levels in the Trivalent Lanthanide Aquo Ions III Tb(III). Absorption Spectra. *J. Chem. Phys.* **1968**, *49* (10), 4447-4449.
81. Carnall, W. T.; Fields, P. R.; Rajnak, K., Electronic Energy Levels in the Trivalent Lanthanide Aquo Ions I. Pr(III), Nd(III), Pm(III), Sm(III), Dy(III), Ho(III), Er(III) and Tm(III). *J. Chem. Phys.* **1968**, *49* (10), 4424-4442.
82. Aebischer, A.; Gummy, F.; Bünzli, J.-C. G., Intrinsic quantum yields and radiative lifetimes of lanthanide tris(dipicolinates). *Phys. Chem. Chem. Phys.* **2009**, *11* (9), 1346-53.
83. Bünzli, J.-C. G.; Chauvin, A.-S.; Kim, H. K.; Deiters, E.; Eliseeva, S. V., Lanthanide Luminescence Efficiency in Eight- and Nine-coordinate Complexes: Role of the Radiative Lifetime. *Coord. Chem. Rev.* **2010**, *254* (21-22), 2623-2633.
84. Blackburn, O. A.; Tropiano, M.; Sørensen, T. J.; Thom, J.; Beeby, A.; Bushby, L. M.; Parker, D.; Natrajan, L. S.; Faulkner, S., Luminescence and upconversion from thulium(III) species in solution. *Phys. Chem. Chem. Phys.* **2012**, *14* (38), 13378-84.
85. Kofod, N.; Arppe-Tabbara, R.; Sørensen, T. J., Electronic Energy Levels of Dysprosium(III) ions in Solution. Assigning the Emitting State and the Intraconfigurational 4f-4f Transitions in the Vis-NIR Region and Photophysical Characterization of Dy(III) in Water, Methanol, and Dimethyl Sulfoxide. *J. Phys. Chem. A* **2019**, *123* (13), 2734-2744.
86. Wei, H.; Zhao, Z.; Wei, C.; Yu, G.; Liu, Z.; Zhang, B.; Bian, J.; Bian, Z.; Huang, C., Antiphotobleaching: A Type of Structurally Rigid Chromophore Ready for Constructing Highly Luminescent and Highly Photostable Europium Complexes. *Adv. Func. Mater.* **2016**, *26* (13), 2085-2096.
87. Ganapathi, M.; Eliseeva, S. V.; Brooks, N. R.; Soccol, D.; Fransaer, J.; Binnemans, K., Electrodeposition of luminescent composite metal coatings containing rare-earth phosphor particles. *J. Mater. Chem.* **2012**, *22* (12), 5514-5522.
88. Binnemans, K., Interpretation of europium(III) spectra. *Coord. Chem. Rev.* **2015**, *295* (0), 1-45.
89. Tanner, P. A.; Yeung, Y. Y.; Ning, L., What Factors Affect the 5D0 Energy of Eu3+? An Investigation of Nephelauxetic Effects. *J. Phys. Chem. A* **2013**, *117* (13), 2771-2781.
90. Frey, S. T.; Horrocks Jr., W. d., On Correlating the Frequency of the F-7(0)->D-5(0) Transition in Eu(3+) Complexes with the Sum of 'Nephelauxetic Parameters' for all of the Coordinating Atoms. *Inorg. Chim. Acta* **1995**, *229*, 383-390.
91. Werts, M. H. V.; Jukes, R. T. F.; Verhoeven, J. W., The emission spectrum and the radiative lifetime of Eu3+ in luminescent lanthanide complexes. *Phys. Chem. Chem. Phys.* **2002**, *4* (9), 1542-1548.
92. Wartenberg, N.; Raccurt, O.; Bourgeat-Lami, E.; Imbert, D.; Mazzanti, M., Multicolour Optical Coding from a Series of Luminescent Lanthanide Complexes with a Unique Antenna. *Chem. Eur. J.* **2013**, *19* (10), 3477-3482.
93. Sizov, V. S.; Komissar, D. A.; Metlina, D. A.; Aminev, D. F.; Ambrozovich, S. A.; Nefedov, S. E.; Varaksina, E. A.; Metlin, M. T.; Mislavskii, V. V.; Taydakov, I. V., Effect of ancillary ligands on visible and NIR luminescence of Sm(3+) beta-diketonate complexes. *Spectrosc. Acta A* **2020**, *225*, 117503.
94. Doffek, C.; Wahsner, J.; Kreidt, E.; Seitz, M., Breakdown of the energy gap law in molecular lanthanoid luminescence: the smallest energy gap is not universally relevant for nonradiative deactivation. *Inorg. Chem.* **2014**, *53* (7), 3263-5.
95. Wahsner, J.; Seitz, M., Perdeuterated 2,2'-bipyridine-6,6'-dicarboxylate: an extremely efficient sensitizer for thulium luminescence in solution. *Inorg. Chem.* **2013**, *52* (23), 13301-3.
96. Yakovliev, A.; Ziniuk, R.; Wang, D.; Xue, B.; Vretik, L. O.; Nikolaeva, O. A.; Tan, M.; Chen, G.; Slominskii, Y. L.; Qu, J.; Ohulchanskyy, T. Y., Hyperspectral Multiplexed Biological Imaging of Nanoprobes Emitting in the Short-Wave Infrared Region. *Nanoscale Research Lett.* **2019**, *14* (1), 243.
97. Li, H.; Wang, X.; Huang, D.; Chen, G., Recent advances of lanthanide-doped upconversion nanoparticles for biological applications. *Nanotechnology* **2020**, *31* (7), 072001.

98. Faustino, W. M.; Malta, O. L.; Teotonio, E. E. S.; Brito, H. F.; Simas, A. M.; De Sá, G. F., Photoluminescence of Europium(III) Dithiocarbamate Complexes: Electronic Structure, Charge Transfer and Energy Transfer. *J. Phys. Chem. A* **2006**, *110* (7), 2510-2516.
99. Bünzli, J.-C. G.; Eliseeva, S. V., Lanthanide NIR luminescence for telecommunications, bioanalyses, and solar energy conversion. *J. Rare Earths* **2010**, *28* (6), 824-842.
100. Winkless, L.; Tan, R. H. C.; Zheng, Y.; Motevalli, M.; Wyatt, P. B.; Gillin, W. P., Quenching of Er(III) luminescence by ligand C-H vibrations: Implications for the use of erbium complexes in telecommunications. *Appl. Phys. Lett.* **2006**, *89* (11), Art. 111115.
101. Ye, H. Q.; Peng, Y.; Li, Z.; Wang, C. C.; Zheng, Y. X.; Motevalli, M.; Wyatt, P. B.; Gillin, W. P.; Hernández, I., Effect of Fluorination on the Radiative Properties of Er<sup>3+</sup> Organic Complexes: An Opto-Structural Correlation Study. *J. Phys. Chem. C* **2013**, *117* (45), 23970-23975.
102. Hernández, I.; Gillin, W. P., Organic Chromophores-Based Sensitization of NIR-Emitting Lanthanides: Toward Highly Efficient Halogenated Environments. In *Handbook on the Physics and Chemistry of Rare Earths*, Bünzli, J.-C. G.; Pecharsky, V. K., Eds. Elsevier: 2015; Vol. 47, pp 1-100.
103. Suffren, Y.; Golesorkhi, B.; Zare, D.; Guenee, L.; Nozary, H.; Eliseeva, S. V.; Petoud, S.; Hauser, A.; Piguet, C., Taming Lanthanide-Centered Upconversion at the Molecular Level. *Inorg. Chem.* **2016**, *55* (20), 9964-9972.
104. Nonat, A.; Chan, C. F.; Liu, T.; Platas-Iglesias, C.; Liu, Z.; Wong, W. T.; Wong, W. K.; Wong, K. L.; Charbonniere, L. J., Room temperature molecular up conversion in solution. *Nature Comm.* **2016**, *7*, 11978.
105. Beeby, A.; Clarkson, I. M.; Dickins, R. S.; Faulkner, S.; Parker, D.; Royle, L.; de Sousa, A. S.; Williams, J. A. G.; Woods, M., Non-radiative deactivation of the excited states of europium, terbium and ytterbium complexes by proximate energy-matched OH, NH and CH oscillators: an improved luminescence method for establishing solution hydration states. *J. Chem. Soc. Perkin Trans. 2* **1999**, 493-503.
106. Melo, L. L. L. S.; Castro, G. P., Jr.; Goncalves, S. M. C., Substantial Intensification of the Quantum Yield of Samarium(III) Complexes by Mixing Ligands: Microwave-Assisted Synthesis and Luminescence Properties. *Inorg. Chem.* **2019**, *58* (5), 3265-3270.
107. Zhang, K.; Lin, M.-L.; Feng, C.-C.; Nie, P.-P.; Yang, Z.-R.; Chen, T.-T.; Zhang, L.-F.; Ma, S.; Shen, Y.-J.; Lu, Z.-Y., The efficient sensitization of Sm(III) ion by a macrocycle with the matched cavity and energy level. *Polyhedron* **2019**, *173*, 114133.
108. Zhang, K.; Lu, Z. Y.; Feng, C. C.; Yang, Z. R.; Nie, P. P.; Chen, T. T.; Zhang, L. F.; Ma, S.; Shen, Y. J.; Lin, M. L., Series of Highly Luminescent Macrocyclic Sm(III) Complexes: Functional Group Modifications Together with Luminescence Performances in Solid-State, Solution, and Doped Poly(methylmethacrylate) Film. *ACS Omega* **2019**, *4* (19), 18334-18341.
109. Kruck, C.; Nazari, P.; Dee, C.; Richards, B. S.; Turshatov, A.; Seitz, M., Efficient ytterbium near-infrared luminophore based on a nondeuterated ligand. *Inorg. Chem.* **2019**, *58* (10), 6959-6965.
110. Ning, Y. Y.; Tang, J.; Liu, Y. W.; Jing, J.; Sun, Y. S.; Zhang, J. L., Highly luminescent, biocompatible ytterbium(III) complexes as near-infrared fluorophores for living cell imaging. *Chem. Sci.* **2018**, *9* (15), 3742-3753.
111. Hu, J.-Y.; Ning, Y.; Meng, Y.-S.; Zhang, J.; Wu, Z.-Y.; Gao, S.; Zhang, J.-L., Highly near-IR emissive ytterbium(III) complexes with unprecedented quantum yields. *Chem. Sci.* **2017**, *8* (4), 2702-2709.
112. Shavaleev, N. M.; Scopelliti, R.; Gumy, F.; Bünzli, J.-C. G., Benzothiazole- and Benzoxazole-Substituted Pyridine-2-Carboxylates as Efficient Sensitizers of Europium Luminescence. *Inorg. Chem.* **2009**, *48* (13), 6178-6191.
113. Bünzli, J.-C. G.; Chauvin, A.-S.; Vandevyver, C. D. B.; Song, B.; Comby, S., Lanthanide Bimetallic Helicates for *in vitro* Imaging and Sensing. *Ann. NY Acad. Sci.* **2008**, *1130* (1), 97-105.
114. Trivedi, E. R.; Eliseeva, S. V.; Jankolovits, J.; Olmstead, M. M.; Petoud, S.; Pecoraro, V. L., Highly Emitting Near-Infrared Lanthanide "Encapsulated Sandwich" Metallacrown Complexes with Excitation Shifted Toward Lower Energy. *J. Am. Chem. Soc.* **2014**, *136* (4), 1526-1534.



A sandwich-type metallacrown has been found to sensitize visible, near-infrared, or dual-range emissions from 10 lanthanide(III) ions. Synthesis, structural analysis and extensive photophysical characterization are presented.